The Generation of Linear and Nonlinear Internal Waves Forced by Subinertial Tides over the Yermak Plateau, Arctic Ocean

GABIN H. URBANCIC,[a] KEVIN G. LAMB,[b] ILKER FER,[c] AND LAURIE PADMAN[d]

[a] *Meteorological Research, Finnish Meteorological Institute, Helsinki, Finland*
[b] *Department of Applied Mathematics, University of Waterloo, Waterloo, Ontario, Canada*
[c] *Geophysical Institute, University of Bergen, Bergen, Norway*
[d] *Earth and Space Research, Corvallis, Oregon*

ABSTRACT: The propagation of internal waves (IWs) of tidal frequency is inhibited poleward of the critical latitude, where the tidal frequency is equal to the Coriolis frequency (f). These subinertial IWs may propagate in the presence of background vorticity, which can reduce rotational effects. Additionally, for strong tidal currents, the isopycnal displacements may evolve into internal solitary waves (ISWs). In this study, wave generation by the subinertial K_1 and M_2 tides over the Yermak Plateau (YP) is modeled to understand the linear response and the conditions necessary for the generation of ISWs. The YP stretches out into Fram Strait, a gateway into the Arctic Ocean for warm Atlantic-origin waters. We consider the K_1 tide for a wide range of tidal amplitudes to understand the IW generation for different forcing. For weak tidal currents, the baroclinic response is predominantly at the second harmonic due to critical slopes. For sufficiently strong diurnal currents, ISWs are generated and their generation is not sensitive to the range of f and stratifications considered. The M_2 tide is subinertial yet the response shows propagating IW beams with frequency just over f. We discuss the propagation of these waves and the influence of variations of f, as a proxy for variations in the background vorticity, on the energy conversion to IWs. An improved understanding of tidal dynamics and IW generation at high latitudes is needed to quantify the magnitude and distribution of turbulent mixing, and its consequences for the changes in ocean circulation, heat content, and sea ice cover in the Arctic Ocean.

KEYWORDS: Internal waves; Solitary waves; Tides; Arctic; Continental shelf/slope; Diapycnal mixing

1. Introduction

The presence of perennial sea ice over the Arctic Ocean is possible due to the insulation of the cold and low-salinity surface water from the warmer and saltier waters below (Carmack et al. 2015). This insulation occurs because of strong near-surface salinity stratification and generally weak upward turbulent heat fluxes. Most of the central Arctic Ocean below the surface layer experiences turbulence levels that are much lower than at midlatitudes (Levine et al. 1985; Padman and Dillon 1987; Rainville and Winsor 2008; Timmermans et al. 2008; Fer 2009). This results in vertical heat fluxes that are typically $O(1)$ W m^{-2} or less. Close to and over the continental slopes, turbulence levels increase to values more typical of the global ocean (Lenn et al. 2022). These slope regions often coincide with pathways for topographically constrained large-scale circulations carrying warm and saline waters. Turbulent mixing leads to water mass transformations as relatively low-salinity shelf waters are modified and meet distinct water masses resident in the deep basins. Understanding how turbulence is generated around the Arctic margins is, therefore, necessary for quantifying heat exchange and mixing in the Arctic and their effects on sea ice cover.

In the global ocean, most of the energy for mixing comes from internal wave (IW) breaking at the end of a cascade of energy facilitated by nonlinear wave–wave interactions through a broadband IW spectrum (Munk and Wunsch 1998; Wunsch and Ferrari 2004; MacKinnon et al. 2017). Observations have shown that the IW spectrum in the central Arctic Ocean is typically characterized by lower IW energy levels, weaker nonlinear interactions, and a richer vertical wavenumber content compared to the midlatitudes (Levine et al. 1985; D'Asaro and Morison 1992). This possibly explains the weak turbulent mixing in the region (Fer 2009; Lenn et al. 2022).

The two main mechanisms for IW generation are wind forcing at the ocean surface and tidal flow over topography. Tidal forcing is the source of around 50% of the IW energy (Waterhouse et al. 2014; Munk and Wunsch 1998). A high-concentration sea ice pack limits the near-inertial wave generation by time-variable wind stress (Martini et al. 2014; Dosser and Rainville 2016). It has been hypothesized by Rainville and Woodgate (2009) that the observed climatological decrease in Arctic sea ice cover would increase the wind-forced IW energy content, potentially enhancing the vertical mixing across the pycnocline. Some observational studies have reported increased dissipation rates in the pycnocline in response to strong wind forcing (Fer 2014; Meyer et al. 2017); however, others did not (Lincoln et al. 2016). Fine and Cole (2022) showed an increase in IW energy but no associated enhancement in dissipation, as the IW vertical length scales compensate to minimize the increase in shear. The pathway of near-inertial wave energy to dissipation is complex and affected by the presence of thin surface mixed layers and strong upper-ocean stratification from low-salinity water (Guthrie and Morison 2021). Tidal flow over topography is expected to continue to be a significant source of mixing in the

---

Corresponding author: G. Urbancic, gabin.urbancic@fmi.fi

Arctic, although their overall contribution may change with the changing Arctic conditions (Fer et al. 2020; Rippeth et al. 2015).

Tidal flow over topography drives mixing through generation of internal tides (ITs), i.e., waves of tidal frequency, and other IWs that can become unstable through shear or convective instabilities (e.g., Thorpe 2021; Zhang and Alford 2015), either locally or after propagating some distance from the source (Whalen et al. 2020). Typically, most of the energy conversion is into ITs (Garrett and Kunze 2007). The principal tidal variable is the cross-slope component of the barotropic tidal current over the sloping or rough seabed. In the Arctic, the modeled maximum cross-slope barotropic tidal current along the continental slope varies from negligible for much of the western Arctic to >0.2 m s^{-1} in many regions of the eastern Arctic (Fer et al. 2020). Tidal currents in the Arctic Ocean not only exhibit a complex spatial pattern, but also vary in their mixture of the dominant tidal species, the semidiurnal and diurnal tides (e.g., Figs. 2–5 in Kowalik and Proshutinsky 1993). Additionally, the diurnal tides in the Arctic generate topographic vorticity waves with diurnal period, whose properties are sensitive to stratification and background mean flows (e.g., Kowalik and Proshutinsky 1993; Skarðhamar et al. 2015).

North of the critical latitude for a specific tidal constituent (where the Coriolis frequency and tidal frequency are equal), ITs cannot propagate freely in the absence of horizontal shear flow, which induces a background vorticity. The critical latitude for the dominant semidiurnal M_2 tidal constituent is near 74.5°, and most of the central Arctic Ocean is north of this latitude. The entire Arctic is also well north of the critical latitude of ~30° for diurnal constituents, including the most energetic constituents K_1 and O_1. The only major tide for which most of the Arctic is below the critical latitude is the semidiurnal S_2, with period 12.00 h and a critical latitude of ~85° (Padman and Erofeeva 2004). Therefore, energy propagation in the form of ITs vanishes in most of the Arctic Ocean as it is north of the critical latitude for almost all tidal constituents. This reduction in freely propagating ITs reduces the total IW energy in the central Arctic, which is already weakened by sea ice reducing energy input via wind forcing (Rainville and Woodgate 2009; Dosser and Rainville 2016; Dosser et al. 2021). IW energy levels in the Arctic Ocean are therefore lower than at midlatitudes, where the ITs are a large component of the energy available for mixing in the deep ocean (Munk and Wunsch 1998).

While ITs cannot propagate freely poleward of their critical latitude, higher-frequency nonlinear IWs generated by subinertial tidal flows (where the tidal frequency is less than the Coriolis frequency) have been observed in several locations. This phenomenon was first studied for the Kuril Straits by Nakamura et al. (2000) for the diurnal K_1 tide. They showed that the K_1 tide interacts with sills to form trapped depressions in their lee, which increase in amplitude and are released upstream when the current slackens. Similar generation mechanisms were studied for the M_2 tide in the Barents Sea (Vlasenko et al. 2003; Kurkina and Talipova 2011; Rippeth et al. 2017) and in the Kara Sea (Morozov and Paka 2010; Morozov et al. 2017).

Vlasenko et al. (2003) modeled the generation of internal solitary waves (ISWs; see section 3); however, they moved the latitude 4° equatorward to reduce f, as a proxy for the negative background vorticity observed in the region. Through numerical experiments, Rippeth et al. (2017) showed that high-frequency nonlinear waves accounted for about 70% of the total tidal conversion over Spitsbergen Bank (at 75.5°N), a shallow bank south of Svalbard about 100 km north of the critical latitude, and are therefore the main source of energy for mixing outside of the bottom boundary layer. Observations north of Svalbard showed a significant increase in local mixing due to ISWs generated by the K_1 tide (Fer et al. 2020). The observed nonlinear waves appear to be partially responsible for the increase in IW energy levels and turbulent dissipation near the continental shelf. The highest observed dissipation occurred along the continental slope north of Svalbard (at ~82°N), although similar magnitudes have been observed over the Yermak Plateau (Rippeth et al. 2015; D'Asaro and Morison 1992).

In addition to numerical studies and in situ measurements, the sea ice retreat in the Arctic has provided new opportunities for remote sensing of ISWs using high-resolution synthetic aperture radar (SAR). Surface signatures of ISW packets have been frequently observed in the Laptev Sea (Kozlov et al. 2017) as far north as 83°N, with most packets appearing north of the critical latitude for the M_2 tide. The location of the observed waves coincide with mixing hot spots and their origin was attributed to lee-wave generation by semidiurnal tides, the dominant tide in the region. ISWs observed in oceanographic data north of Svalbard were also captured in SAR images (Fer et al. 2020). The emerging observations emphasize the importance of nonlinear IWs for vertical mixing in the Arctic Ocean.

As a representative site for nonlinear wave generation by strong subinertial tidal currents and due to the significance of the Yermak Plateau (YP) for the Arctic Ocean, we study IW generation over the YP for both the semidiurnal and diurnal tides using a high-resolution, two-dimensional nonlinear model. The importance of the YP and observations over its north flank are presented in section 2. Section 3 provides a background on IWs relevant to interpreting the results of the numerical simulations. The numerical model used in this work is presented in section 4. As the observations show variability in the amplitude of cross-isobath diurnal currents, we ran simulations for a wide range of tidal amplitudes (section 5). Weak amplitude semidiurnal tides are considered in section 6. Simulations with a large range of Coriolis frequencies were undertaken as a proxy for background vorticity. The sensitivity of ISW generation by diurnal tides to changes in stratification, topography, and Coriolis frequency are discussed in section 7. Our discussion and conclusions are presented in sections 8 and 9, respectively.

2. Observations over the Yermak Plateau

The YP is a bathymetric feature stretching out into Fram Strait northwest of Svalbard (Fig. 1). It plays a prominent role in the Arctic's heat balance due to its interaction with
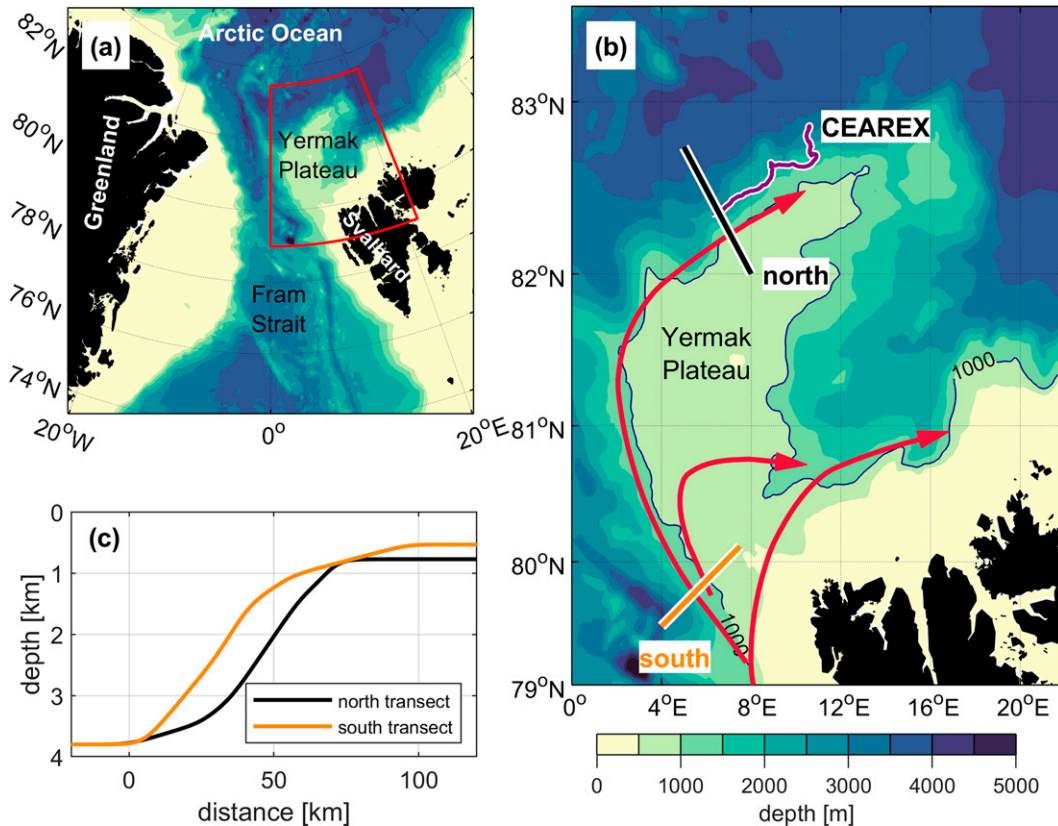
FIG. 1. Bathymetric map of (a) Fram Strait and (b) the Yermak Plateau. The main circulation patterns of the warm Atlantic Water are indicated. The track of the CEAREX drift camp and the location of the north and south transects implemented in the model are shown. (c) The topography along the north and south transect. Horizontal distance is measured relative to the base of the slope.

the West Spitsbergen Current, which is the main contributor to heat transport into the central Arctic Ocean (Aagaard et al. 1985). The YP is the last obstacle between the West Spitsbergen Current and the Arctic, and regions downstream of the YP are noted for significant cooling of the West Spitsbergen Current (Kolås et al. 2020). The marginal ice zone at the Polar Front typically extends across the YP, resulting in high variability in sea ice cover and significant local exchange between the ocean and atmosphere (Onarheim et al. 2014).

Spatial and temporal variability of the diurnal currents over the YP is significant. Their amplitudes have been observed to increase by over an order of magnitude over the YP in comparison to observations in the Arctic basin (Padman et al. 1992). The largest current amplitude was observed over the upper slope and not on the top of the plateau, suggesting more complicated dynamics than amplification by cross-isobath volume conservation. The location of this maximum is consistent with a simple model of barotropic, topographic vorticity waves of diurnal frequency (Hunkins 1986; Padman et al. 1992). These diurnal waves are generated at the eastern side of the YP where they are resonantly amplified as the group velocity is zero. This amplification increases the tidal conversion as the current ellipses have a large

cross-isobath component, forcing a stronger baroclinic response than would otherwise occur. Observations on the northern flank of the YP have characterized the region as one of enhanced IW activity and nonlinear IWs have been observed (Czipott et al. 1991; Padman and Dillon 1991; Padman et al. 1992). The effects of nonlinear waves generated over the YP are important as they can modulate and force mixing processes (Padman and Dillon 1991; Wijesekera et al. 1993a,b).

Observations of tidal forcing and its link to finescale and small-scale variability are scarce over the northern YP, where the diurnal currents are amplified. The location is typically ice covered, making observations logistically difficult. The most complete dataset from this region was collected from the Coordinated Eastern Arctic Experiment (CEAREX) Oceanography Camp drifting on the pack ice along the northern slope of the YP (Fig. 1) in April 1989. Instruments on ice-tethered moorings measured currents and hydrographic variables at fixed depths. Profiles of temperature, salinity and turbulent dissipation rates were obtained 2–3 times per hour from the surface to about 300–400-m depth. Tiltmeters on the ice surface measured ice flexure.

The dominant signal of variability was diurnal oscillations, which forced isopycnal displacements and cross-slope currents
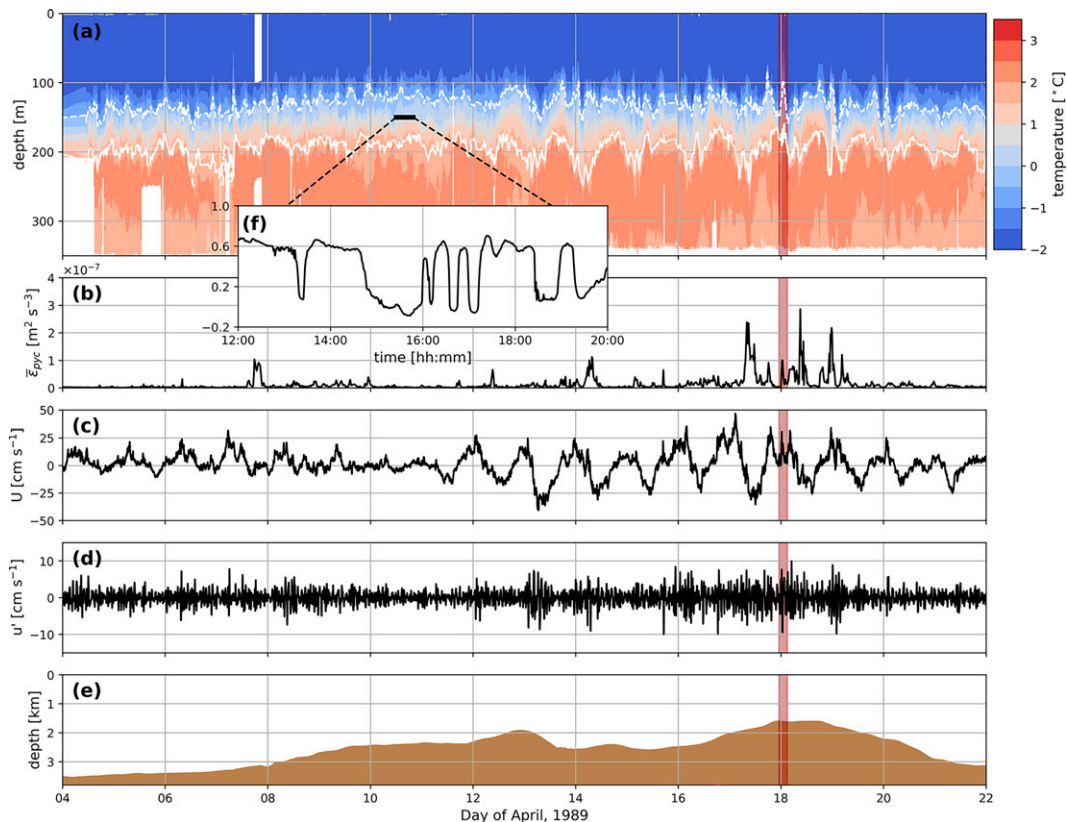
FIG. 2. Observations along the CEAREX drift track (see Fig. 1). The interval studied in Czipott et al. (1991) is highlighted in red. (a) The temperature measured by the profiling instrument, with pycnocline outlined (in white) by the −0.5° and 1.7°C isotherms; (b) pycnocline-averaged dissipation rate $\bar{\epsilon}_{pyc}$; (c) the cross-slope velocity U measured at the 150-m depth; (d) the bandpassed (8–60 min) cross-slope velocity u' measured at the 150-m depth; (e) the water depth along the CEAREX drift track; and (f) the temperature measured at the 150-m depth for an 8-h interval marked in (a).

(Figs. 2a,c). Padman et al. (1992) noted that the ice response at diurnal periods was small, which they attributed to internal ice stresses in the convergent sea ice pack in the region. The diurnal signals in the ocean were largest when the camp drifted along the central continental slope near the 2000-m isobath. Based on a barotropic tide model (Padman and Erofeeva 2004), much of this variability is spatial; however, Padman et al. (1992) also estimated a significant contribution from spring–neap variability as the K_1 and O_1 tides interact. High dissipation rates, signifying energetic turbulent mixing in the pycnocline, were also diurnally modulated (Fig. 2b), although with substantial higher-frequency variability as well, including at ∼2 and ∼4 cycles per day (Padman et al. 1991).

Additional signals, consistent with ISWs, were also found. Using tiltmeters, Czipott et al. (1991) measured ice flexure forced by an energetic packet of IWs as the camp drifted near the 2000 m isobath. They noted the presence of an IW packet in the pycnocline about 100-m depth, with two to three oscillations at periods from 20 to 40 min, that rode on undular bores passing the ice camp location diurnally. An undular bore typically displaced the pycnocline upward by about 15 m.

Observations were consistent with ISWs coming from tidal flow over the YP, propagating roughly north at 0.45 m s^{-1} with a wavelength of about 600 m. These features were also recorded at other times: a short record of temperature at 1-min sampling at 150-m depth shows rapid oscillations of ∼0.8°C during 9 April (Fig. 2f), while bandpassed currents (8–60 min) at 150-m depth (Fig. 2d) confirm the presence of ISWs crossing the slope during a much longer time interval than studied by Czipott et al. (1991).

These observations indicate a tidal origin for higher-frequency nonlinear waves that provide the energy for large mixing events (Wijesekera et al. 1993b). These mixing events lead to substantial upward heat transfer from the warm Atlantic Water to the cold Arctic surface water and to the sea ice above. These observations motivate our idealized numerical experiments to better understand the nonlinear IW response from tidal forcing over the YP. The CEAREX observations captured the processes in early spring, when the surface mixed layer was deep and the upper ocean stratification was weak (see Fig. 3). As we expect a stronger nonlinear IW response for stronger and shallower stratification, we base our main experiments on summer stratification.
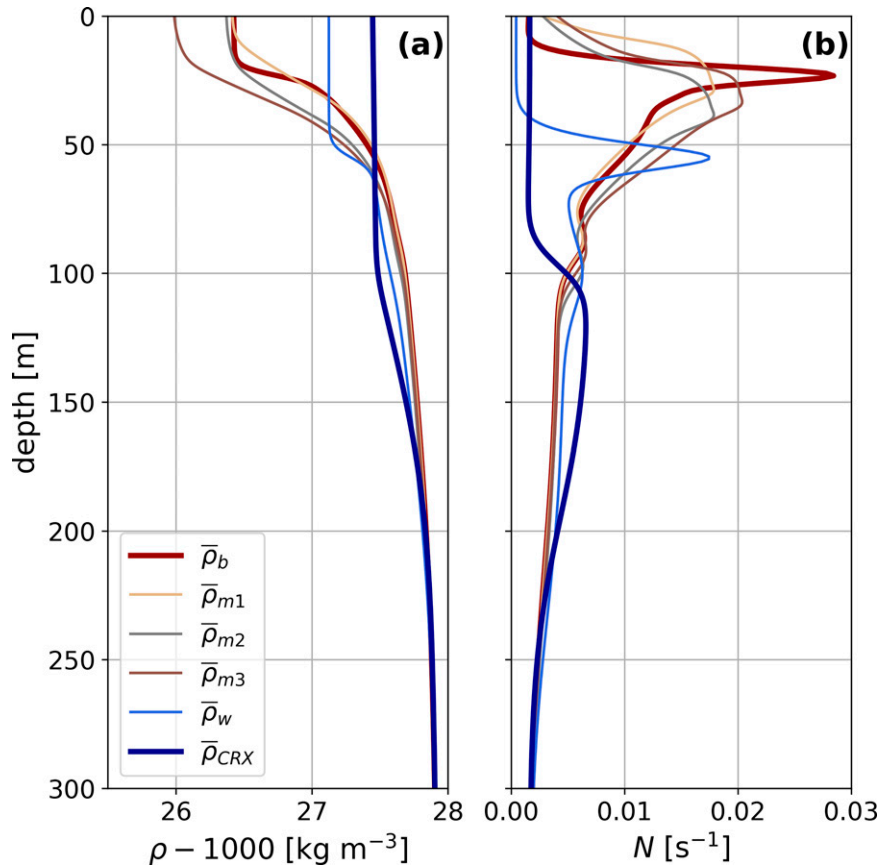
FIG. 3. Model stratifications. (a) Density profiles and (b) the resulting buoyancy frequency; $\overline{\rho}_b$ (red) is the summer base stratification used in the majority of the simulations, $\overline{\rho}_{mi}$ for $i = (1, 2, 3)$ are three modified summer stratifications, $\overline{\rho}_w$ is a winter stratification, and $\overline{\rho}_{CRX}$ is from the CEAREX observations.

3. Background

The dynamics of IWs has been extensively studied analytically through the development of both linear and weakly nonlinear theory, as well as numerically for the study of nonlinear IWs. In this section, we present the IW theory relevant to the interpretation of the simulation results and present the parameter space of IWs at high latitudes. For additional information on IWs in the ocean, see Garrett and Munk (1979). Helfrich and Melville (2006) review the literature on nonlinear IWs, and for more on the effects of rotation, see Grimshaw et al. (1998). A thorough review specifically on ITs is presented by Garrett and Kunze (2007).

In the absence of background currents, linear IWs on a traditional *f*-plane obey the dispersion relation

$$\omega^2 = \frac{N^2 k^2 + f^2 m^2}{k^2 + m^2} \qquad (1)$$

in the vertical *x*–*z* plane, where ω, N, and f are the intrinsic wave, buoyancy, and Coriolis frequencies, respectively, and (k, m) is the wavenumber vector. The Coriolis frequency is equal to $2\Omega\sin(\phi)$, where Ω is the rotation rate of Earth

$(7.2921 \times 10^{-5} \text{ s}^{-1})$ and ϕ is the latitude. As the YP lies in the Northern Hemisphere we assume $f > 0$ below. The horizontal component of Earth's rotation is neglected in the traditional approximation, but can become important in the deep ocean for poleward propagating ITs (Gerkema and Shrira 2005).

From the dispersion relation (1), it follows that the angle of energy propagation depends only on ω for fixed N and f. If the topographic slope forces fluid parcels oscillating at frequency ω to move in the direction of energy propagation, then the response is resonant and the most efficient generation occurs. This is characterized by the criticality parameter

$$\alpha(z) = \left| \frac{dh}{dx}(z) \right| \times \left[\frac{N^2(z) - \omega^2}{\omega^2 - f^2} \right]^{1/2}, \qquad (2)$$

which is the ratio of topographic slope to the slope of energy propagation (Legg 2014; Garrett and Kunze 2007). The slope is said to be subcritical, critical, and supercritical when $\alpha < 1$, $\alpha = 1$, and $\alpha > 1$, respectively. At critical slopes, intense IW beams emanating from the slope are generated even under weak tidal flow conditions (Gerkema et al. 2004; Garrett and Kunze 2007). For sufficiently subcritical topographies, the

response is primarily the first vertical mode IT and generation over the whole slope contributes to the energy input. In contrast, supercritical topographies generate many vertical modes; however, the energy flux from high mode waves is small. The most significant generation occurs at the shelf break, where the tidal currents are strongest and the topography is often close to critical (Baines 1982).

Linear theory (Bell 1975; Khatiwala 2003) for subcritical, small-amplitude topography, with constant N (assuming $N > f$, a normal condition in the ocean), predicts that tidal flow will generate propagating waves of all the tidal harmonics that lie in the frequency band

$$f < \omega < N. \tag{3}$$

These theories are for small topographic features, with the same water depth on either side, and assume periodic solutions; therefore, only waves of the tidal harmonic frequencies are present. Bell (1975) considered a semi-infinite domain and included harmonics outside the freely propagating frequency band, which decayed exponentially with height. The case of a finite depth ocean with a rigid upper boundary was considered by Khatiwala (2003), who ignored waves outside of the freely propagating frequency band as they make no contribution to the energy flux. Lamb and Dunphy (2018) extended Khatiwala's method to include variable stratification and surface trapped currents for $f = 0$. The important dimensionless parameter for wave propagation is the ratio ω_T/f, where ω_T is the frequency of tidal constituent T. When $\omega_T/f > 1$ (superinertial) and $\omega_T/N < 1$, inequality (3) holds and the ITs are freely propagating. When $\omega_T/f < 1$ (subinertial), the tidal frequency response is forced and the ITs decay exponentially away from the generation site. In the subinertial regime, freely propagating higher harmonics satisfying (3) are generated with the lowest harmonic satisfying (3) dominating the response.

The latitude at which $\omega_T/f = 1$ is called the critical latitude of tidal constituent T. It is also referred to by some authors as the turning latitude as poleward-propagating ITs are reflected equatorward at this latitude (Garrett 2001). Not only does the existence of a critical latitude imply no generation of propagating ITs north of it, but it also acts as a filter for northward-propagating ITs. As ITs approach their critical latitude the group velocity approaches zero and the phase velocity approaches infinity, continuously adopting the evanescent response which occurs north of the critical latitude. Background vorticity, introduced by the presence of a horizontal shear flow, can supplement or counter the planetary vorticity modifying the lower bound of (3) from f to the effective Coriolis frequency

$$f_{\text{eff}} = \sqrt{f^2 + f\zeta} \approx f + \frac{1}{2}\,\zeta, \tag{4}$$

where $\zeta = (\partial V_b/\partial x) - (\partial U_b/\partial y)$ is the background vorticity (Mooers 1975; Kunze 1985). This provides a commonly referenced mechanism (e.g., Vlasenko et al. 2003) for the propagation of the ITs north of the critical latitude as the modified propagating wave band is $f_{\text{eff}} < \omega < N$.

An important parameter for IW generation by tidal flow is $\delta = kU_T/\omega_T$, where k is a horizontal wavenumber and U_T is the barotropic tidal amplitude. The horizontal wavenumber k can be interpreted as an inverse length scale of the topography in which case δ is a measure of the ratio of the tidal excursion distance U_T/ω to a topographic length scale. When $\delta \ll 1$ the generated waves are predominantly of tidal frequency. As the tidal current strengthens, δ becomes larger, and the higher harmonics make an increasingly important contribution. Topographic features include a range of length scales, or wavenumbers k. In the following sections, we only present values of δ where the topographic length scale is chosen as the width of the shelf slope, which we denote as δ_L.

Nakamura et al. (2000) introduced the idea of unsteady lee waves for $\delta \gg 1$ and mixed tidal–lee waves for $\delta \sim 1$. They argued that waves with a continuous range of k values were generated as the tidal current varied and that these waves had an intrinsic Doppler-shifted frequency $\pm\omega_T + kU_T$; however, Tanaka et al. (2010) pointed out an error in their derivation and showed that the intrinsic frequency is kU_T, i.e., the lee wave frequency (Legg 2021). The strongest generation occurs near peak tidal currents as these currents are approximately steady for the longest period of time (Nakamura and Awaji 2001; Mohri et al. 2010). Because these waves are generated periodically, in the case of small-amplitude topography they are included in the previously cited linear theories. Linear theory for large-amplitude topographic features, including shelf-like topography, assume the barotropic tidal current is so weak that tidal excursion distances are negligible and only waves of tidal frequency are generated (Baines 1982; Gerkema et al. 2004; Mathur et al. 2016). Wave frequencies at interharmonic frequencies can arise due to transient effects, e.g., due to an impulsive startup which will generate waves of all frequencies, or due to nonlinearities associated with supercritical and/or large-amplitude topography. An example of the latter is the generation of subtidal frequency waves via parametric subharmonic instability (PSI) and higher-frequency interharmonic waves through nonlinear wave–wave interactions (Korobov and Lamb 2008; Bourget et al. 2013).

Sufficiently strong tidal currents can generate ISWs. ISWs are nonlinear dispersive waves that are commonly observed in the ocean, particularly in coastal waters where they are predominantly generated by tidal flow over topography. They are typically generated by the nonlinear dispersive evolution of the internal tide or by the generation of nonlinear lee waves (Jackson et al. 2012). At subinertial latitudes they may also be generated by the nonlinear evolution of large elevations or depressions of isopycnal surfaces, typically formed over a shelf slope (Vlasenko et al. 2003). At mid-to-high latitudes, rotation results in a gradual decay in their amplitude due to the backward radiation of long inertia–gravity waves (Helfrich 2007).

4. Numerical model and model setup

To simulate IW generation by tidal flow over topography, we solve the 2D, nonlinear, nonhydrostatic, Boussinesq equations

on an f plane (Lamb 1994; Lamb and Dunphy 2018). The model equations are

$$\mathbf{U}_t + \mathbf{U} \cdot \nabla \mathbf{U} - f v \hat{\mathbf{x}} = -\frac{1}{\rho_0} \nabla p - \frac{\rho g}{\rho_0} \hat{\mathbf{z}} \tag{5}$$

$$v_t + \mathbf{U} \cdot \nabla v + fu = 0 \tag{6}$$

$$\rho_t + \mathbf{U} \cdot \nabla \rho = 0 \tag{7}$$

$$\nabla \cdot \mathbf{U} = 0, \tag{8}$$

where $\mathbf{U} = (u, w)$ is the 2D velocity in the vertical x–z plane, represented by the $\hat{\mathbf{x}}$ and $\hat{\mathbf{z}}$ unit vectors, v is the along slope velocity, ρ is the density, ρ_0 the reference density, and g is the acceleration of gravity. The cross-slope velocity can be decomposed as $U = U_T + u'$, where $U_T(x, t)$ is the vertically averaged barotropic velocity and u' is the baroclinic velocity. No variation occurs in the along-slope direction (i.e., $\partial/\partial y = 0$) maintaining the 2D approach while allowing for rotation. The model uses a second-order, finite volume projection method with Godunov flux limiting which acts as an implicit large-eddy simulation (LES) filter (Bell and Marcus 1992; Margolin et al. 2006; Lamb and Dunphy 2018). A rigid lid is applied at the surface ($z = 0$) and the bottom boundary is at $z = -H + h(x)$ where $H = 3800$ m is the deep water depth and $h(x)$ the shelf topography. The model uses terrain following coordinates, increasing the vertical resolution in shallower waters. We used 300 grid points in the vertical. To resolve a narrow near-surface pycnocline, Δz varies between 25 m below 500 m to slightly smaller than 2 m in depths less than 120 m in the deep water and between 14 and 1 m on the plateau. Both lateral boundaries are open, and the tide is forced at the left boundary, resulting in a volume-flux-conserving barotropic flow. All IWs reaching the left boundary would be reflected while long hydrostatic waves pass through the right boundary; however, short nonhydrostatic waves will be reflected. To eliminate wave reflection the horizontal resolution is varied, with a resolution of 30 m in a 700-km-wide central domain and a gradually decreasing resolution beyond. This resolves waves in the region of interest while ensuring that IWs never reach the lateral boundaries. Higher-resolution simulations were conducted to verify that this resolution was adequate. The full fields were saved 48 times per tidal period.

Artificial mooring lines were placed in positions of interest; along these lines, velocity and density fields were saved at every time step. Both Eulerian and Lagrangian moorings are considered, where Eulerian moorings are fixed in space and Lagrangian moorings save values in a reference frame moving with the barotropic tide. We only present results from Lagrangian moorings as they remove aliasing of the baroclinic signal due to advection by the barotropic tide.

We consider two transects, referred to as the south and north transects (Figs. 1b,c). As the Coriolis frequency varies only slightly across the plateau, the f-plane approach is justified and unless otherwise specified was set to $f = 1.44 \times 10^{-4}$ s^{-1}, corresponding to 80.9°N which lies between the two transects. Other values were used to test the sensitivity of the

results on the value of f, which corresponds to changes in latitude. Changing the latitude is used as a proxy for the presence of background vorticity which modifies the dispersion relation (1) and by consequence the lower bound of (3) to f_{eff}. The focus of this work is on the north transect as ISWs have been observed in this region (see section 2).

Simulations were initiated at maximum flood tide by setting the initial fields to

$$(u, v, w) = \left(\frac{Q}{H - h(x)}, 0, -\frac{Qh'(x)}{[H - h(x)]^2} z \right), \tag{9a}$$

$$\rho = \overline{\rho}(z), \tag{9b}$$

where $Q = U_0 H$ is the peak volume flux, U_0 is the barotropic tidal amplitude in the deep water away from the topography, and $\overline{\rho}(z)$ is a prescribed background density profile. The tidal flow is forced by the left boundary condition,

$$\frac{\partial u}{\partial t} = -\omega_T U_0 \sin(\omega_T t), \tag{10}$$

where ω_T is the tidal frequency (where $T = \text{M}_2$ or K_1). Some simulations were run starting from rest with the tidal amplitude ramped up over 4 or 8 tidal periods. This reduced the amplitudes of transient linear waves but did not significantly affect ISW generation.

Figure 3 shows the upper 300 m of all the stratifications used in this study. For most simulations, we use a representative stratification for summer conditions with a 15-m surface mixed layer, the pycnocline at 30 m with $N_{\text{max}} = 0.028$ s^{-1} and a deep ocean stratification of $N = 0.002$ s^{-1}. This summer stratification is referred to as the "base stratification" and is denoted by $\overline{\rho}_b$. It was derived from summer profiles collected during the cruises on board the R/V *Håkon Mosby* (cruise numbers 2007-613, 2014-619, and 2015-617); the 2007 data are reported by Fer et al. (2010), and the 2015 data are reported by Kolås and Fer (2018). Three modified summer stratifications ($\overline{\rho}_{mi}$ for $i = 1, 2, 3$), with much broader pycnoclines based on climatology (Steele et al. 2001), are used to explore the sensitivity to the width and depth of the pycnocline. Additionally, we explore two stratifications based on winter conditions. The CEAREX stratification ($\overline{\rho}_{\text{CRX}}$) is based on observations during the CEAREX field program (Padman and Dillon 1991) while an additional winter stratification ($\overline{\rho}_w$) is based on Steele et al. (2001). Below 300 m depth, all stratifications profiles are the same, representative of the cruise data and the September climatology (Steele et al. 2001) with N decreasing monotonically to about 6×10^{-4} s^{-1} at $z = -1500$ m. N is about 5.5×10^{-4} s^{-1} below $z = 2000$ m. Unless otherwise specified the base stratification is used.

The barotropic tidal amplitudes (Table 1) over the YP are extracted from the Arctic Ocean Tidal Inverse Model (AOTIM-5; Padman and Erofeeva 2004). For comparison, values are also presented from a newer, higher-resolution model covering the YP, the Greenland 1 km Tide Model (Gr1kmTM; Howard and Padman 2021). The Gr1kmTM on-shelf diurnal currents are 2–3 times larger than in AOTIM-5 for the north

Table 1. The AOTIM-5 and Gr1kmTM derived cross-slope tidal amplitudes (cm s^{-1}) for the north and south transect over the shelf break and over the deep basin.

	AOTIM-5				Gr1kmTM			
	M_2	S_2	K_1	O_1	M_2	S_2	K_1	O_1
North transect								
Shelf break	2.4	0.9	12.0	8.7	2.6	0.9	34.2	15.7
Deep basin	0.9	0.3	1.6	1.2	0.9	0.3	4.9	1.8
South transect								
Shelf break	6.7	2.3	7.7	3.1	7.3	2.5	10.8	9.5
Deep basin	2.7	1.0	2.7	1.0	3.2	1.1	3.8	3.4

transect. For both models, the strongest tidal constituents over the YP are diurnal K_1 and O_1 tides and the semidiurnal M_2 tide. The spring–neap cycle for the diurnal tide is around 14 days. For simplicity we only consider M_2 and K_1 tides in isolation. In both tidal models, the kinetic energy in K_1 is dominated by energy in topographic vorticity waves which cannot be represented in a 2D model. Since our primary focus is to represent cross-slope currents over the shelf break, we artificially adjust deep-water tidal currents from $U_0 = 0.023$–0.23 m s^{-1}, which generates upper-slope currents within the range observed by Padman et al. (1992). We use 23.93 h for the K_1 tidal period and 12.42 h for the M_2 tidal period.

Additional simulations were run with the gravitational acceleration set to zero to determine the evolution of the density field due to tidal and rotational affects only, i.e., without the effects of gravitational restoring forces. In the following results, time is reported in terms of the tidal period T for the tidal constituent under consideration.

5. Diurnal tide

In this section we present the model results for the K_1 tide. We begin by considering a case with weak deep water tidal currents with amplitude $U_0 = 0.023$ m s^{-1}. The resulting barotropic current over the shelf has an amplitude of $U_s = 0.113$ m s^{-1}, which is 6% less than the AOTIM-5 tidal amplitude at the shelf break (Table 1). The values of δ_L ranges from 0.03 to 0.13, computed for the deep and shelf currents, respectively. The largest generated waves are transient waves associated with the impulsive startup (not shown). The maximum isopycnal displacement in the water column is about 0.3 and 0.5 m for waves propagating in the on-shelf and off-shelf directions, respectively. The amplitude of the propagating waves is small compared to the tidal heaving over the shelf slope, which has an isopycnal displacement of around 50 m.

The baroclinic horizontal velocity field (u') at $t = 40T$ is shown in Fig. 4a. The most notable feature is the pattern of coherent IW beams emanating from the shelf break. Characteristics of the second harmonic frequency $2\omega_{K_1}$, which is larger than f, are included showing that these beams are largely of that frequency. A range of higher-frequency waves are also visible as steeper beams in a fan-like structure above the second harmonic on-shelf beam. Power spectra from the

artificial moorings (Figs. 4b,c) show clear peaks at $2\omega_{K_1}$. The slightly steeper beams, which reach $x = 110$ km between 50- and 200-m depths, have a frequency of about $2.07\omega_{K_1}$. The third and fourth harmonic beams are also apparent in the response over the shelf. This can be seen at $x = 84$ km where the fourth harmonic beam reflects from the surface, and at $x = 88$ km where the third harmonic can be seen propagating down from the surface. The offshore propagating response has weaker higher harmonic content with the third harmonic beam reflecting off the surface at $x = 60$ km. As N/ω_{K_1} ranges from around 30 to 400 the most energetic harmonics propagate freely.

Although the barotropic currents are forced at frequency ω_{K_1}, it is the $2\omega_{K_1}$ frequency which has the largest energy in the baroclinic field with smaller peaks at ω_{K_1}, $3\omega_{K_1}$ and at higher harmonics (Figs. 4b,c). The peak at ω_{K_1} occurs because the tidal currents force an evanescent response at this frequency which decays with distance from the shelf slope. The e-folding decay scales for the off-shelf and on-shelf mode-1 response are 8.1 and 5.5 km, respectively, computed by solving the nonhydrostatic rotational linear eigenvalue problem for mode-1 waves (Kundu 1990). These decay scales are consistent with the decay observed in the spectra from the artificial moorings.

Figure 5 shows the frequency that is critical for the slope at a given depth. The second harmonic is critical on the slope near the shelf break, where tidal currents are large, resulting in the efficient generation of second harmonic IW beams. Slope criticality of the second harmonic of the K_1 tide appears to be an important parameter for IW generation at high latitudes.

As the generated IWs are linear for the small tidal amplitude case ($U_0 = 0.023$ m s^{-1}), the enhanced diurnal currents due to resonant topographic vorticity waves is a good candidate for the generation of ISWs observed over the YP. To investigate the baroclinic response to the stronger forcing, we consider a range of larger tidal currents with a maximum deep-water current of $U_0 = 0.23$ m s^{-1}.

Results from the $U_0 = 0.23$ m s^{-1} case, for which δ_L ranges from 0.26 to 1.34, are presented in Fig. 6. The density field at $t = 3T$ shows large ISWs with displacements up to 73.5 m. Evidently a significant regime transition occurs in the wave generation between $U_0 = 0.023$ and 0.23 m s^{-1}. Two main disturbances propagate in both the on-shelf and off-shelf directions. The disturbances propagating off-shelf are ISWs marked L_1 and L_2. The on-shelf disturbances are an ISW packet marked R_1 and an ISW marked R_2. The isopycnal displacements further from the shelf slope are waves generated during the previous tidal periods. The vertical structures of L_1, L_2, R_1, and R_2 are shown in Fig. 6b. The maximum displacement of the isopycnals occurs at around 50-m depth. The ISW solutions of the Dubreil–Jacotin–Long (DJL) equation (Stastna and Lamb 2002) show that, for ISWs with an amplitude of 50 m, the maximum displacement has a depth of about 40 m. The ISWs observed in Fig. 6 are therefore consistent with the ISW solutions of the DJL equation. In contrast, the linear long-wave vertical eigenmode has its maximum displacement at a depth of about 200 m.
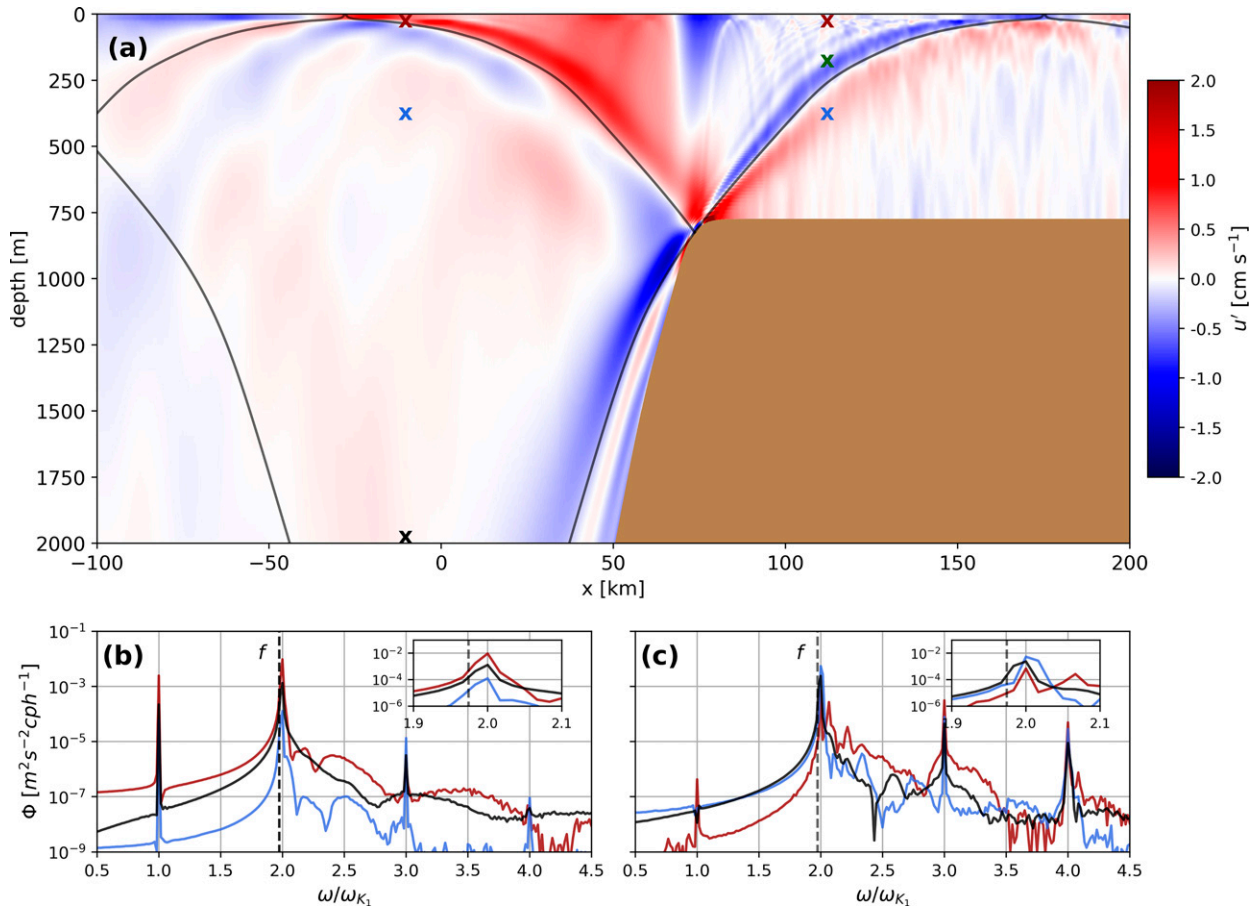
FIG. 4. Simulation results of the K_1 tide for $U_0 = 0.023$ m s^{-1}. (a) The baroclinic horizontal velocity, u', at $t = 40T$, the power spectra of u' from artificial Lagrangian moorings (lasting 60 tidal periods) for (b) off-shelf and (c) on-shelf mooring lines placed at $x = -12.5$ and 110 km, respectively. Red and blue are the 50 and 400 m depth moorings, respectively. Black and green are the 2000 and 200 m depths for the off-shelf and on-shelf moorings, respectively. The "x" marks in (a) show the mooring positions. The black lines in (a) are the ray paths for frequency $2\omega_{K_1}$. The dashed line in (b) and (c) shows the Coriolis frequency.

The evolution of these waves is presented in Fig. 7b using the displacement of the isopycnal with the undisturbed depth at 50 m. All four disturbances are generated every tidal period (TP), except during the first two TPs which are affected by the initial rest state and the impulse start. The generation of the ISWs is the result of three processes: upwelling and downwelling by the vertical barotropic velocity, horizontal advection, and gravitational/rotational adjustment. On the shelf, the barotropic tidal current has an amplitude of 1.13 m s^{-1} resulting in a particle excursion distance of 15.5 km. In deeper water at $x = 60$ and 70 km (1400 and 925 m depth) the particle excursion distances are about 8.6 and 12.9 km. These are large enough to play an important role in the evolution of the isopycnal.

The quasiperiodic generation mechanism is illustrated in Fig. 7d, which shows a waterfall plot of the isopycnal surface relative to the undisturbed level at 50-m depth (light horizontal lines). The stages of wave generation are marked chronologically A–F. At $t = 2T$ (peak flood tide), the isopycnal over the upper shelf ($x = 70$ km) is slightly elevated above its initial

height (A). This elevation builds in amplitude while it is being advected on-shelf by the barotropic tide. At the start of ebb tide ($t = 2.25T$) elevation A is propagating off-shelf. Its trailing edge has steepened, resulting in a local minimum (B) slightly above the undisturbed height (for the equivalent simulations using $g = 0$, not shown, the isopycnal has a single local maximum at $x = 73$ km at the start of ebb tide). In the first TP this minimum is also present at this location but is less pronounced. During ebb tide, the local minimum B is advected off-shelf and it becomes apparent that it is an off-shelf propagating wave. It steepens to form wave L_2. Meanwhile, the elevation to the right of this depression (C) is advected off-shelf by the barotropic current and the associated downwelling results in the formation of a local depression in the middle of it (D). This depression splits into off-shelf and on-shelf propagating depressions. The off-shelf propagating depression is larger, and steepens to form wave L_1. Meanwhile, the on-shelf propagating depression (E) steepens to form wave R_2. At $t = 2.625T$ the flow is still off-shelf and the downwelling barotropic tidal current results in a new depression (F) located
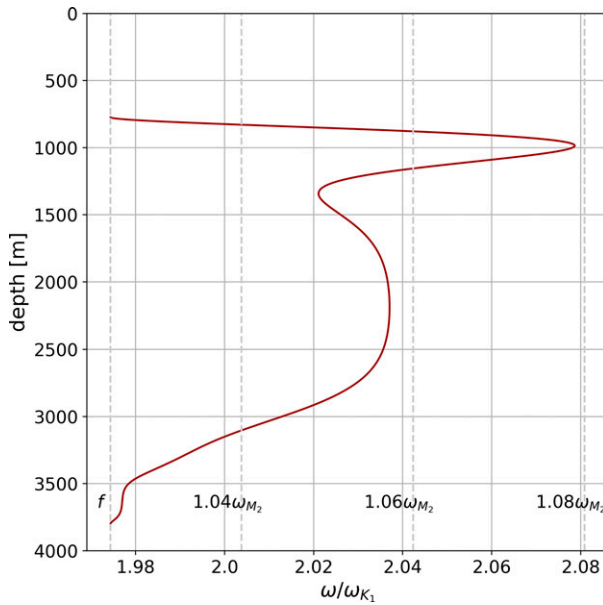
FIG. 5. Frequency for which the slope of the north transect is critical as a function of depth for the base stratification. The dashed vertical lines indicate the Coriolis frequency and select multiples of the M_2 tidal frequencies.

at $x = 63$ km which develops until the end of ebb tide [for the equivalent simulations using $g = 0$, the isopycnal has a single local minimum which is located at $x = 62$ km. It is only a few meters smaller than depression (F)]. It then evolves into wave packet R_1. The asymmetry in the location of the maximum at the start of ebb tide ($t = 2.25T$) and the minimum at the start of flood tide ($t = 2.75T$) in the simulation with $g = 0$ can be ascribed to strong horizontal advection by the barotropic tidal currents.

To better understand the transition from a linear ($U_0 = 0.023 \, \text{m s}^{-1}$) to a nonlinear wave regime ($U_0 = 0.23 \, \text{m s}^{-1}$) in which ISWs are generated, a set of simulations were run with intermediate values of U_0. Figure 8a shows the 50-m isopycnal for four values of U_0 and Fig. 8b shows the dependence of the amplitudes of L_1, L_2, R_1, and R_2 on U_0. The features of L_1, R_1, and R_2 are considered at $t = 2T$ and L_2 at $t = 2.5T$ due to their different times of generation and their increasingly ephemeral nature as the tidal current decreases. We chose not to consider later tidal periods as the isopycnals are complicated by previously generated waves and become harder to identify for weaker values of U_0.

The $U_0 = 0.115 \, \text{m s}^{-1}$ case exhibits none of the ISWs generated in the $0.23 \, \text{m s}^{-1}$ case although a hint of R_1 is seen. The regime is very weakly nonlinear. By $U_0 = 0.138 \, \text{m s}^{-1}$ the R_1 packet is established and disperses into a train of ISWs propagating past $x = 250$ km by $t = 4T$. Hints of L_2 and R_2 are also seen. This is followed by a transition at around $U_0 = 0.15 \, \text{m s}^{-1}$, where R_2 is established as an ISW and L_1 and L_2 are observed. This is followed by the rapid development of L_1 whose amplitude grows after $U_0 = 0.17 \, \text{m s}^{-1}$ and becomes the second largest feature after R_1.

For all tidal amplitudes the off-shelf waves are more transient than the on-shelf waves. For example, for $U_0 = 0.184 \, \text{m s}^{-1}$, wave L_2 is only present between $1.4T$ and $1.7T$ during the second tidal period and between $2.3T$ and $2.9T$ during the third tidal period. In contrast, both R_1 and R_2 are observed for multiple tidal periods. This can be explained by a combination of rotational effects and depth changes. Both R_1 and R_2 are generated on the shelf and therefore propagate through an area with constant depth. The off-shelf waves are generated over the slope and therefore experience a large increase in depth that modulates their vertical structure.

In Fig. 8c the available potential energy (APE) of wave L_1, L_2, the leading wave in wave packet R_1, and wave R_2 are plotted as functions of U_0. The energies were integrated over a minimal domain that spanned the wave using the initial density as the reference density profile (Lamb and Nguyen 2009). At times that are multiples of half a tidal period, as used here, the mean heights of all isopycnals resume their initial values so use of the initial density profile is appropriate. The kinetic energy (KE) of the waves were not calculated directly because of the difficulty of the nonlinear dependence of the KE on the currents associated with ISWs and the currents associated with other waves upon which they are superimposed. These include the trapped ITs of ω_{K_1} frequency, as the generation site of the ISWs are in their range of influence, as well has higher tidal harmonic internal waves. ISWs typically have KE/APE between 1 and 1.3 (Lamb and Nguyen 2009), so doubling the APE values provides an estimate of the total energy, approximately 2–15 MJ m^{-1} for the R waves and 4–35 MJ m^{-1} for the L waves. To put these values in some context we compare the APE and KE in domains that are just large enough to contain each of the four wave packets with the total APE and baroclinic KE (459 and 116 MJ m^{-1}, respectively) integrated between $x = -20$ and 140 km. This domain was chosen as it contains all four ISW packets for the base case at $t = 3T$. The location of wave L_1 contains 5.0% of the total KE and 9.7% of the total APE. The corresponding values for the other packets are 3.2% and 11.3% for L_2, 11.9% and 14.6% for R_1, and 1.2% and 4.7% for R_2. The ratio of the KE to APE at the location of the four packets is 2.0, 1.1, 3.2, and 1.0.

6. Semidiurnal tide

No amplification of semidiurnal currents due to topographic vorticity waves has been observed over the YP (Hunkins 1986) and the barotropic currents are weak. In addition to the weak currents, the YP is north of the critical latitude with $\omega_{M_2}/f = 0.98$, implying an evanescent IT. The subinertial ITs are still of interest as observations have recorded energy peaks at ω_{M_2} north of the critical latitude (e.g., Fer et al. 2010). Additionally, generation and propagation at near-inertial latitudes requires special consideration (Garrett 2001).

Simulations over the north transect were run with the deep water tidal amplitude, based on AOTIM-5, of 0.014 m s^{-1} (Fig. 9a). The values of δ_L ranges from 0.01 to 0.04, computed for the deep and shelf currents, respectively. The baroclinic signal (u') is complicated with coherent IW beams emanating from the shelf break, propagating in the on-shelf direction
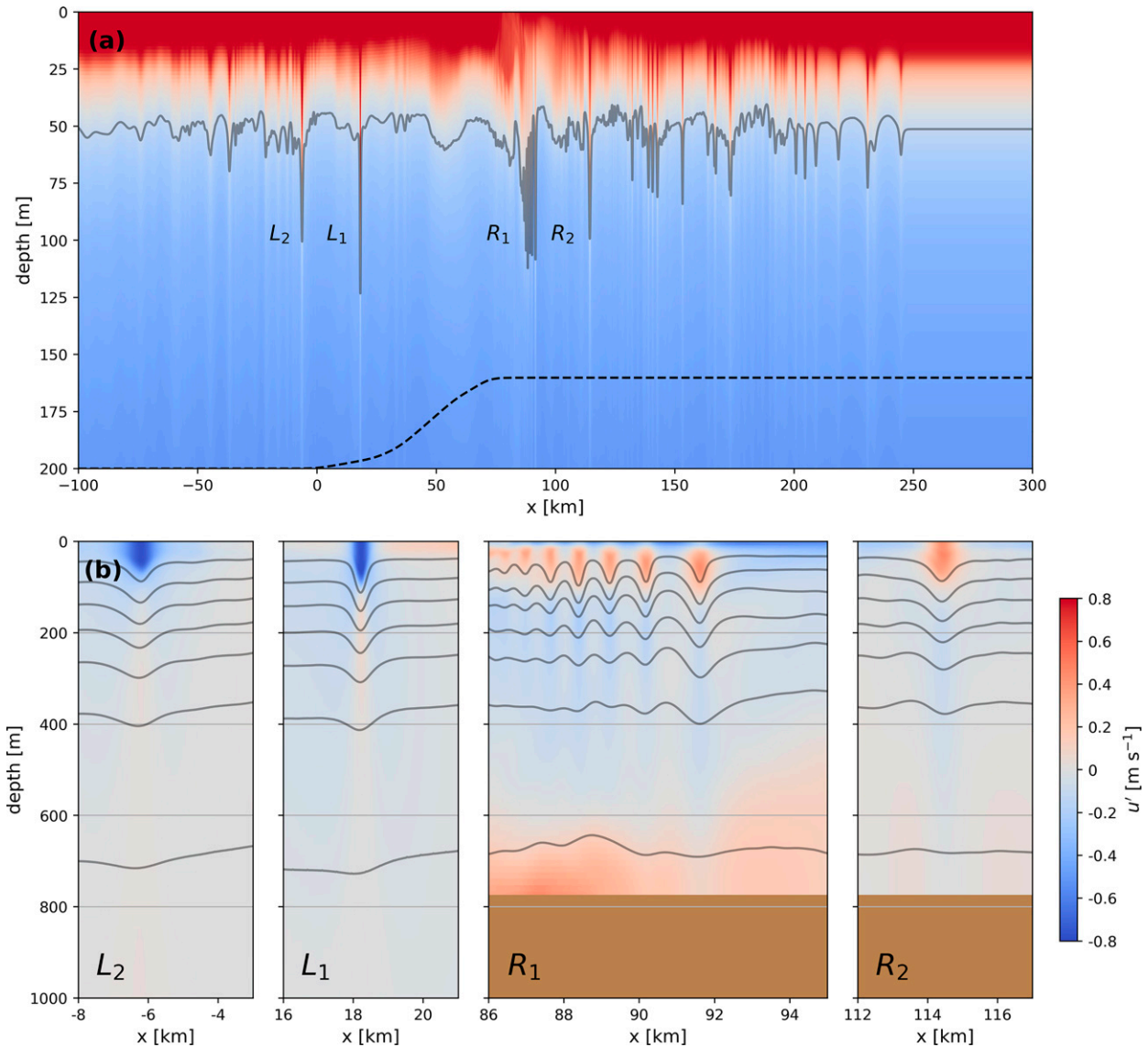
FIG. 6. Simulation results of the K_1 tide for $U_0 = 0.23$ m s^{-1} after three tidal periods. (a) The density field and (b) the baroclinic velocity field for L_2, L_1, R_1, R_2. The solid black line in (a) is the 50-m isopycnal and the black lines in (b) are the density contours. The dashed line in (a) illustrates the position of the topography.

(Fig. 9a). Unlike the K_1 case with a similar tidal amplitude (Fig. 4a), the largest spectral peak is not at the second harmonic. The topography is subcritical with $\alpha < 0.2$ for $2\omega_{M_2}$ (Fig. 5), implying no enhancement of higher harmonics due to critical slopes.

A closer look at the near-inertial spectra (as seen in the subpanels of Figs. 9b,c), shows that both the on-shelf and the off-shelf moorings have spectral peaks at slightly higher frequencies than both the M_2 ($\omega/\omega_{M_2} = 1$) and the Coriolis frequency (dashed line), resulting in their free propagation. Secondary peaks are seen at ω_{M_2} due to the forced, decaying response. The M_2 tide north of the critical latitude forces a propagating response at frequencies just above f. Sample ray paths of frequency $1.07\omega_{M_2}$ plotted in Fig. 9a show the beams

are of slightly superinertial frequencies and well below the second harmonic. This response is not predicted by steady state linear theory which only predicts the generation of tidal harmonics (see section 3). The baroclinic response can therefore be attributed to finite amplitude effects which are not present in $\delta = 0$ theory.

As seen from the power spectra of Fig. 9, the baroclinic horizontal velocity of simulated Lagrangian moorings at different depths have different spectral peaks. The propagating response is therefore a spectrum of frequencies as also seen in the fan-like structure of the beams. Spectra of u' obtained from the mooring on the shelf for multiple depths illustrates the band of frequencies generated (Fig. 10). To account for the varying stratification, the spectra are WKB-scaled using
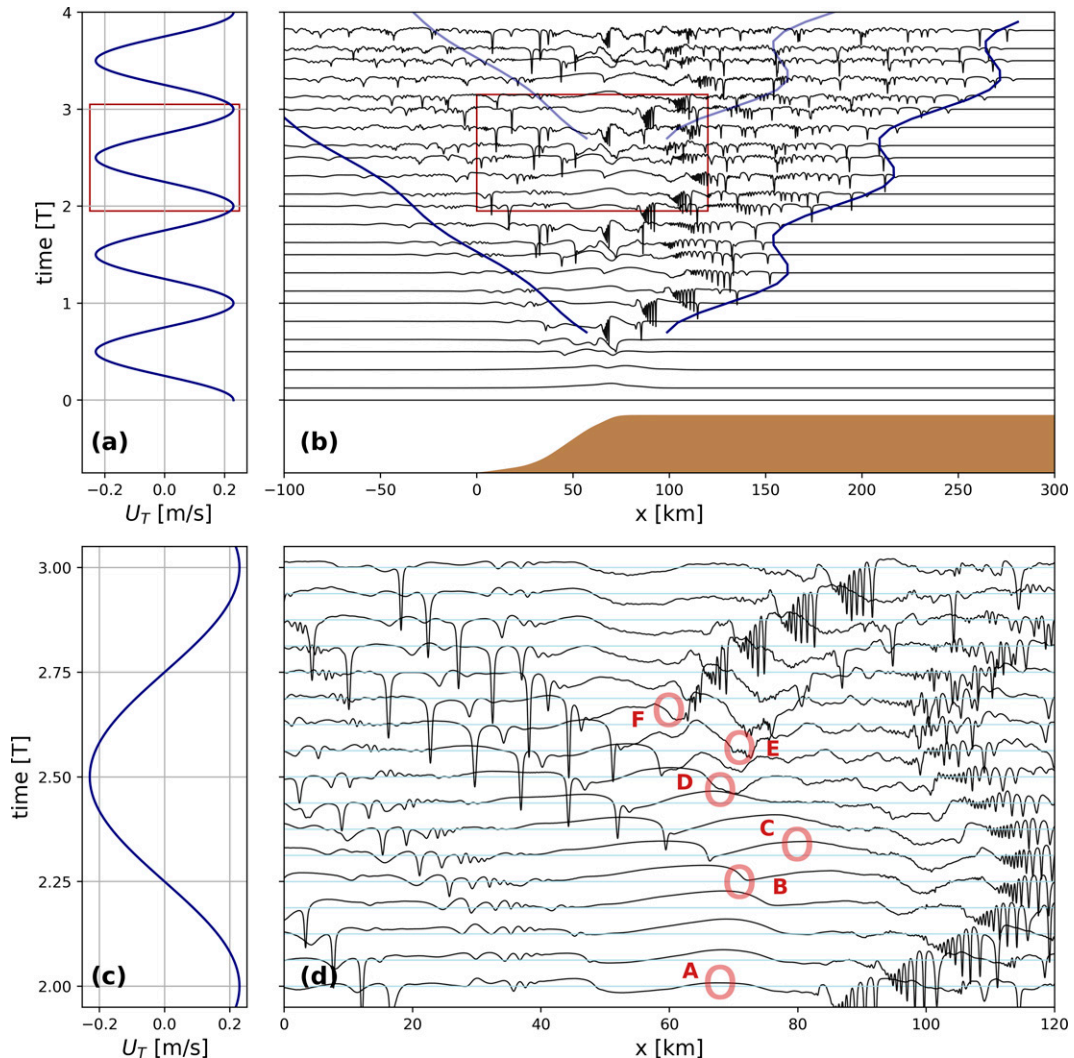
FIG. 7. Simulation results of the K$_1$ tide for $U_0 = 0.23$ m s^{-1}. (a),(c) The deep water barotropic tidal currents; (b) waterfall plot of the 50-m isopycnal; and (d) a zoom in of the waterfall plot. The blue lines in (b) are the wave characteristics for the linear waves with maximum group velocity and the red box shows the zoom in area of (c) and (d). The light blue lines in (d) show the undisturbed height of the isopycnals. See text for a discussion of the wave forms labeled A–F.

$N_0/N(z_m)$, where N_0 is a reference value taken as the deep water stratification, and z_m is the depth of the u' time series (Leaman and Sanford 1975; Smith and Young 2002). Along the north transect topography, the frequencies which have a critical slope have minimum values of $f = 1.025\omega_{M_2}$ at the top and bottom of the shelf where the slope is zero, and maximum values at $1.079\omega_{M_2}$ (Fig. 5). The baroclinic response has spectral peaks in a range of near-inertial frequencies which have critical slopes at the shelf break. Variations in the WKB-scaled spectral peaks can be explained by the variations in the strength of currents at the depths of the critical slopes.

Background vorticity has been observed over the YP by D'Asaro and Morison (1992) with a value of $\zeta = -0.15f$ resulting in $\omega_{M_2}/f_{eff} = 1.05$, i.e., freely propagating waves. This regime is analogous to the f-plane at a latitude of 66°. To better understand the effect of background vorticity on IW generation over the YP, simulations were run for a range of values of f as a proxy for changes in background vorticity (Table 2). The model results for a subset of the f values are presented in Fig. 11. The evolution of the vertically integrated energy flux for the on-shelf and off-shelf propagating waves illustrates the effect of latitude (or equivalently background vorticity). In most cases, the fluxes increase to a maximum value, level off, and start decreasing. This maximum occurs at different times for different latitudes and the evolution is significantly different for the on-shelf and off-shelf fluxes. An initial maximum was reached for all latitudes except at 72° in both the on-shelf and off-shelf directions, and at 67° in the on-shelf direction. To compare the transient fluxes at different latitudes we use the maximum energy flux over the first 40 TP. The maxima,
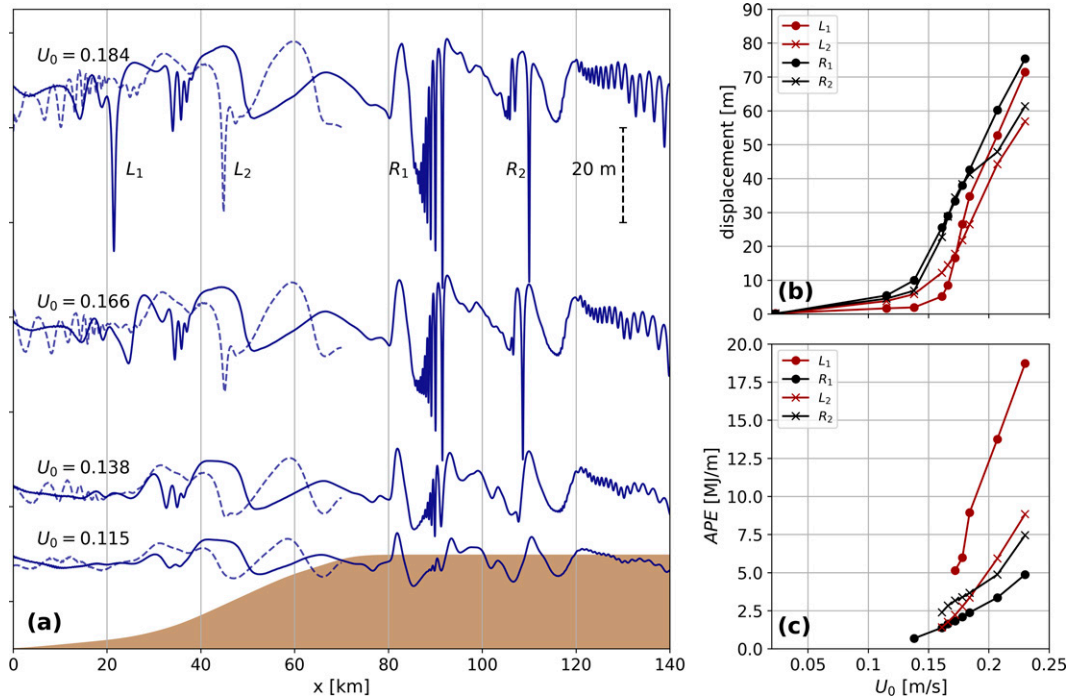
FIG. 8. Simulation results of the K_1 tide for varying U_0 (m s^{-1}). (a) The 50-m isopycnal where the solid lines and dashed lines are after 2 TP and 2.5 TP, respectively. (b) The dependence of amplitudes of different features on U_0 and (c) the dependence of APE on U_0. For (b) and (c) the L_1, R_1, and R_2 are measured at $2T$ while L_2 is measured 1/2 TP later. The amplitudes are measured as the maximum downward displacement of the isopycnals about the rest height.

plotted in Fig. 11c, show the effect of the critical latitude with a rapid decrease in energy flux around 74.5°. This decrease is an underestimate as the maximum is larger at 72°, as it failed to reach the maximum by $t = 40T$. The maximum on-shelf fluxes north of the critical latitude are not very sensitive to latitude. For the background vorticity levels observed by D'Asaro and Morison (1992), the estimated maximum energy flux is increased by an order of magnitude and is therefore a potentially significant spike in IW energy. The maximum u' over the slope increased by a factor of 3, with values of 0.058 and 0.17 m s^{-1} for 81° and 67°, respectively. For the on-shelf flux, the lowest latitude results in the largest energy flux. In contrast, the off-shelf flux has its maximum at a latitude of 70°.

7. Sensitivity of ISW generation

In this section, the sensitivity of the generation of ISWs by the K_1 tide to the topography, stratification, and Coriolis frequency is investigated. We consider the strong current case with $U_0 = 0.23$ m s^{-1}.

To test the sensitivity to the topography, we compare results for the north and south transects (Fig. 1). Along the south transect, the plateau is 240 m shallower than on the north transect, resulting in stronger barotropic currents. Additionally, the southern slope is 25 km wider than the northern slope. The increased slope width is largely due to a weaker slope near the shelf break. The value of δ_L is comparable for

both transects with δ_L ranging from 0.2 to 1.48 and from 0.26 to 1.34 for the south and north transects, respectively.

The results for the two transects are very different: four ISW packets are generated each tidal period for the north transect while none are generated for the south transect. To illustrate the reason for this difference, we compare results of the two transects at $t = 0.25T$ and $0.5T$ (Fig. 12a). A later tidal period is not used because the wave field is simplest in the first tidal period and shows the essential features. At the end of the on-shelf flow ($t = 0.25T$), the displacement of the 50-m isopycnal for the south transect extends 20 km farther than the north transect. This is due to the longer slope and to larger on-shelf tidal currents, which increase the advection distance on the shelf. The maximum displacement of the isopycnal is largest for the north transect as the vertical barotropic current is proportional to the shelf slope, resulting in a larger vertical velocity. An off-shelf propagating elevation anomaly is apparent for the north transect between $x = 55$ and 70 km. This feature is missing in the south transect's isopycnal. After half a tidal period, there are two 10-m depressions at $x = 45$ and 70 km for the north transect which give rise to ISWs L_1 and R_1. This evolution does not occur for the south transect. In summary, tidal heaving at the south transect elevates and depresses the isopycnals over a longer region but with smaller amplitude due to weaker vertical barotropic currents. This results in much weaker nonlinear steepening and consequently no ISWs are formed.

To investigate the sensitivity to the stratification, we use the north transect topography with three alternate summer
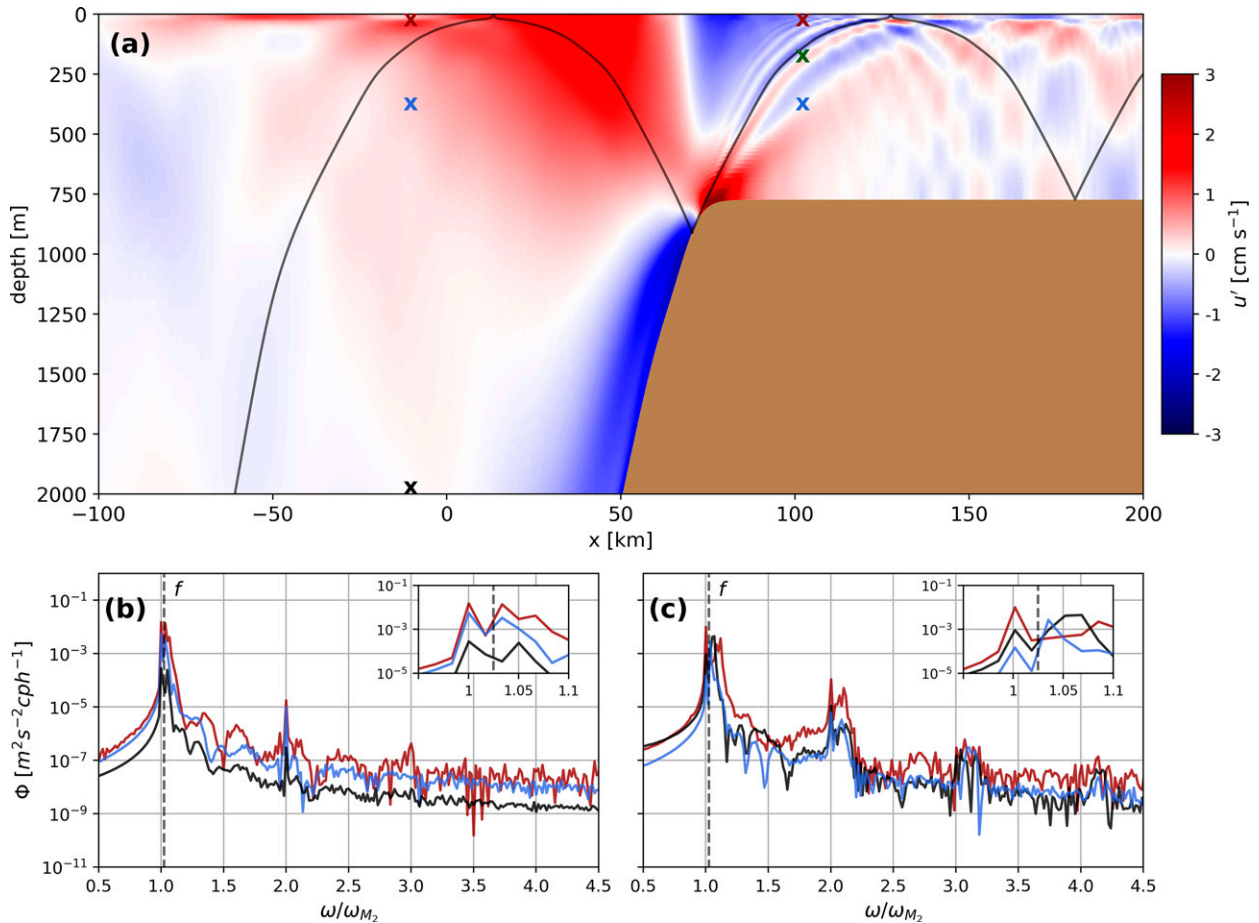
FIG. 9. Simulation results of the M_2 tide for $U_0 = 0.014$ m s^{-1}. (a) The baroclinic horizontal velocity, u', at $40T$, power spectra of u' from artificial Lagrangian moorings (lasting 60 tidal periods) for (b) off-shelf and (c) on-shelf mooring lines placed at $x = -12.5$ and 100 km, respectively. Red and blue are the 50 and 400 m depth moorings, respectively. Black and green are the 2000- and 200-m depths for the off-shelf and on-shelf moorings, respectively. The "x" marks in (a) show the mooring positions. The black lines in (a) are the ray paths for the $1.07\omega_{M_2}$ frequency. The dashed lines in (b) and (c) show the Coriolis frequency.

stratifications and two winter stratifications (see Fig. 3), described in section 4. Figure 12b compares results for the four summer stratifications after three tidal periods. Isopycnals from the same depth are used, so vertical displacement amplitudes will differ due to the thickness and depth ranges of the pycnocline. The four ISW packets are present in all four cases and have similar amplitudes. Stratification $\overline{\rho}_{m3}$, which has the largest density variation across the pycnocline, has the fastest wave propagation speeds with the ISW packets further from the generation site than those in the other cases. In addition, there are two ISWs in packet L_2 for this stratification. For the winter stratifications, with much deeper pycnoclines, isopycnals from different depths are used. Results are best illustrated at $t = 3.75T$ when the four ISWs are all present. The ISWs are much broader and wave packet R_2 now consists of a single ISW. The waves propagate away from the generation site more slowly for the two winter stratifications because of the reduced cross-pycnocline (and hence top to bottom) density variation.

Last, we consider the dependence of ISW generation on the Coriolis frequency. The values considered are presented in Table 3 along with the corresponding value of background vorticity. The largest and smallest of these correspond to about ±10% decrease/increase in f over the YP.

The 50-m depth isopycnal at $t = 3T$ is shown for the five cases in Fig. 13. In all cases ISWs are formed by the same processes that led to waves L_1, L_2, R_1, and R_2 for $f = 1.44 \times 10^{-4}$ s^{-1} (i.e., the base case) and are labeled accordingly. For f between 1.4×10^{-4} s^{-1} and 1.445×10^{-4} s^{-1}, the results are very similar to the base case. The most notable difference is that the single ISW R_1 is now a packet of two waves. This illustrates that the results are not very sensitive to f for the range of f values over the YP. There are some intriguing nonmonotonic behaviors, for example the number of waves in packet L_2. We attribute these to variations in propagation speeds and the spatial decay rate of the subinertial ω_{K_1} response.

For the smallest value of f (Fig. 13e), ISW packet R_2 is similar but has fewer ISWs than the corresponding packet in the base case. At $t = 2.875T$, R_1 consisted of three ISWs, but by $t = 3T$ they have almost disappeared. There are four offshore propagating ISWs which can be separated into two groups,
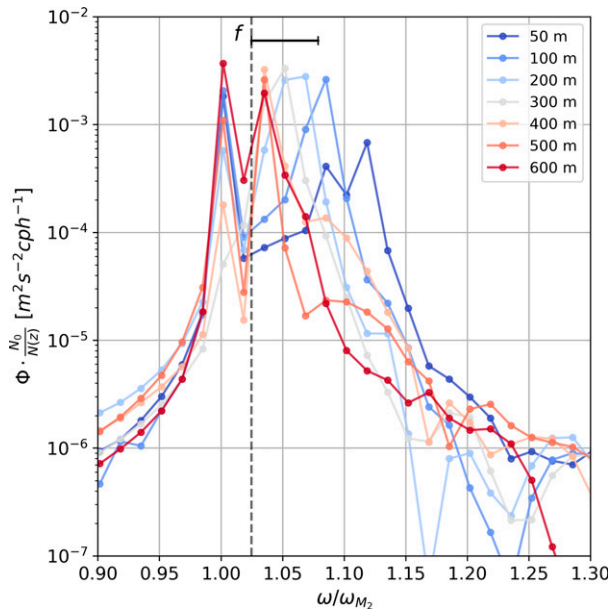
FIG. 10. Scaled Lagrangian power spectra of u' for the on-shelf ($x = 100$ km) mooring line of the M_2 tide simulation with $U_0 = 0.014$ m s^{-1}. The solid black shows the frequency range with critical slopes and the dashed black line is the Coriolis frequency. The spectra are scaled with the WKB scaling $N_0/N(z)$ to make the different depths comparable where $N_0 = 0.002$ s^{-1} represents the deep water stratification.

the first being the leading ISW (L_1) and the second consisting of the trailing three waves which make up ISW packet L_2. Wave L_1 evolves differently than for the base case. A small ISW is initially formed in the same way L_1 is generated in the base case; however, it is small and disappears as a larger ISW forms just behind it. This becomes the leading wave at $x = 12$ km in Fig. 13e. For this f, ISW packet L_2 consists of three ISWs. For the largest value of f (Fig. 13a), wave L_1 is also short lived, as its existence in the third tidal period is limited to the interval $t = 2.375T$ and $2.75T$. The L_2 ISW packet consist of five waves, one at $x = 18$ km and four much smaller waves trailing by about 15 km. The on-shelf wave packets R_1 and R_2 are similar to those in the base case, in particular, there is only one ISW in R_1 in both of these cases.

8. Discussion

The presence of amplified barotropic, cross-slope diurnal currents is a necessary condition for the generation of ISWs over the YP. Simulations with tidal amplitudes comparable to diurnal currents reported by Padman et al. (1992) resulted in the periodic generation of two off-shelf propagating ISWs. These waves have displacements up to 73.5 m with the largest off-shelf propagating ISW carrying 35 MJ m^{-1} of energy. The ISWs are generated by the nonlinear steepening of isopycnals which are displaced by the vertical barotropic velocity. No ISWs were generated for the south transect, which is explained by weaker vertical barotropic currents at the shelf break due to the smaller topographic slope. The amplitude of the vertical barotropic current at the pycnocline is, therefore, a good prognostic for ISW generation.

The modeled barotropic tidal currents increase over the slope due to cross-isobath volume conservation. Observations showed that the maximum diurnal currents occurred over the slope and not on the shelf implying more complex dynamics, consistent with topographic vorticity waves of diurnal frequency. The model is unable to represent these waves, and our increase of the deep-water tidal currents is a proxy for the topographic vorticity waves, as we force similar currents at the shelf break. This approach is justified as the modeled ISWs are consistent with the observations. Observations showed variability in the dissipation rates with a period of 6 h over the 2000-m isobath, which is the time delay between generation of the L_1 and L_2 ISWs. The wavelength was measured at around 600 m, again consistent with the modeled ISW in Fig. 6.

ISW generation over the YP is of interest as it is a region with strong generation from subinertial tidal constituents. For comparison to the ISWs generated over the YP, which reach 35 MJ m^{-1}, ISW energies observed elsewhere range from $O(1)$ MJ m^{-1} on shallow shelves, such as the New Jersey Shelf (Shroyer et al. 2010) and the Washington Shelf (Zhang et al. 2015), to as high as 2 GJ m^{-1} in the much deeper South China Sea basin where the largest ISWs have been observed (Klymak et al. 2006). The presence of these waves provides a supply of energy for mixing through their dissipation as well as resulting in large vertical displacements of density surfaces. The trajectory of the West Spitsbergen Current and its proximity to the ISW generation sites with enhanced mixing can increase heat flux from the warm waters below the mixed layer toward the sea ice above (Padman and Dillon 1991; Fer et al. 2010, 2015).

The model results for the M_2 tide show the generation of IWs in a range of near-inertial frequencies inside the propagating wave band. The dominant response occurred at frequencies with critical slopes near the shelf break. This novel generation mechanism should be included in parameterizations of mixing as it can be important for the ocean's energy balance at high latitudes.

TABLE 2. Values of f used in the sensitivity runs for the M_2 tide, the criticality of the M_2 tide (ω_{M_2}/f), the corresponding latitude, and the background vorticity required over the YP to have f_{eff} equal to f.

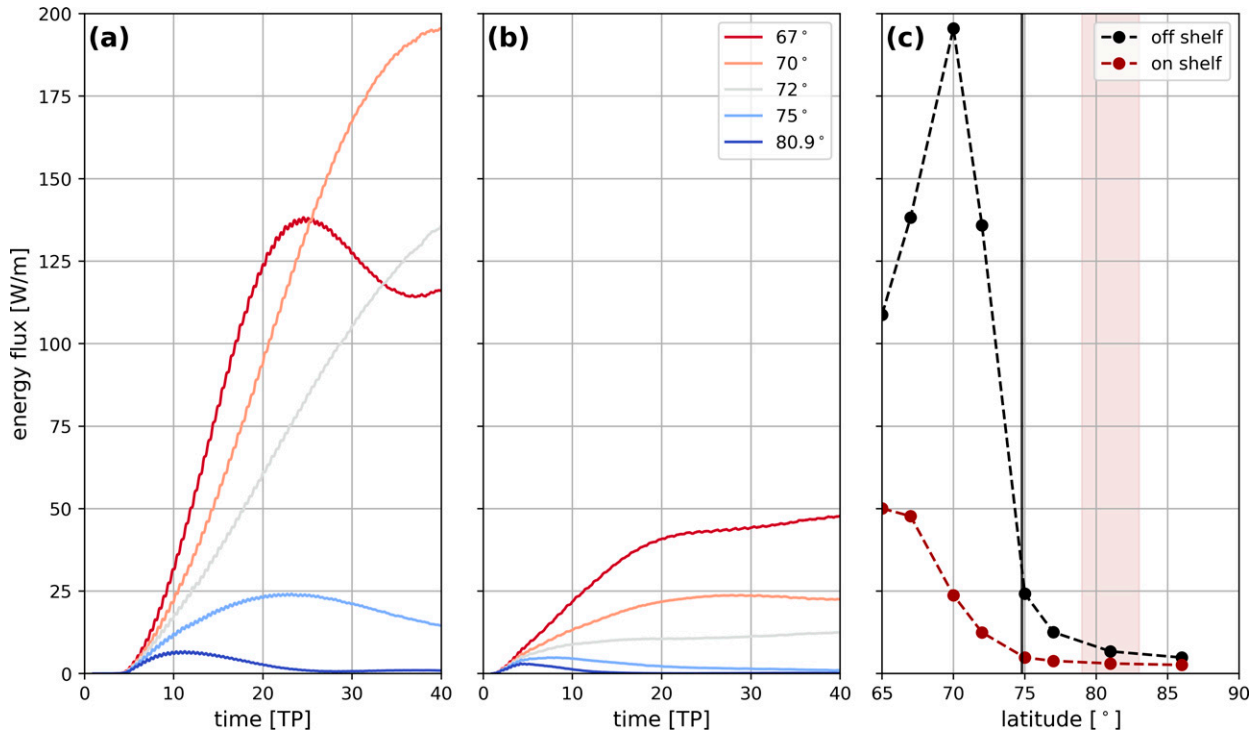| f (s^{-1})	1.32×10^{-4}	1.34×10^{-4}	1.37×10^{-4}	1.39×10^{-4}	1.41×10^{-4}	1.42×10^{-4}	1.44×10^{-4}	1.45×10^{-4}
ω_{M_2}/f	1.065	1.049	1.026	1.011	0.997	0.990	0.976	0.966
Latitude (°)	65	67	70	72	75	77	80.9	86
ζ (s^{-1})	-2.4×10^{-5}	-2.0×10^{-5}	-1.4×10^{-5}	-1.0×10^{-5}	-6.0×10^{-6}	-4.0×10^{-6}	0	2.0×10^{-6}

FIG. 11. Simulation results of the M_2 tide for $U_0 = 0.014$ m s^{-1} and varying f. The time evolution for select cases of the (a) off-shelf and (b) on-shelf vertically integrated energy flux, measured at $x = -50$ and 100 km, respectively. (c) The maximum values during the first $40T$. The vertical black line is the M_2 critical latitude, and the shaded red region is the latitude range of the YP.

For freely propagating waves, the barotropic to baroclinic energy conversion can be analytically estimated using inviscid linear theory. Such theories are used to estimate the global energy conversion to the ITs (Nycander 2005). The tidal frequency response north of the critical latitude is trapped, with zero net conversion in an inviscid flow. Since they only considered waves of tidal frequency, Falahat and Nycander (2015) introduced a damping time scale (3 days) where the energy density in the trapped waves lose energy to frictional effects. The damping results in energy conversion from the barotropic tides. This energy is dissipated locally or propagates along the isobaths, and represents the enhanced turbulent levels near the continental slope around the Arctic Basin. In contrast to linear theories, our numerical results produce propagating waves with a range of frequencies. The propagating response has spectral energy levels of the same order as the trapped waves at tidal frequency (Fig. 10). In the tidal energy conversion and energy flux calculations, both the trapped and propagating response must be considered.

The presence of IWs in the propagating frequency band generated by subinertial tides can cause difficulty in the analysis of mooring spectra. Resolving the near-inertial band is the first difficulty due to the length of time series, T_{obs}, required as the spectral resolution is $1/T_{obs}$. To distinguish the Coriolis frequency at a latitude of 80.9° from ω_{M_2} requires a times series of $40.4T$ (20.9 days). Our simulations of the M_2 tide were run for $60T$ (31 days) resulting in a spectral resolution of $0.017\omega_{M_2}$. This resolution was sufficient for our conclusions

although we were unable to fully resolve the variations in the frequency of all the spectral peaks (Fig. 10). Additionally, frequency alone from moorings is not sufficient information to determine the tidal constituent responsible for their generation. The solar semidiurnal tide (K_2) has $\omega_{K_2}/\omega_{M_2} = 1.035$, a value in the middle of the propagating frequency band generated by the M_2 tide. Propagating waves at the K_2 frequency, observed north of the critical latitude for the M_2 tide, may have been generated by the M_2 tide.

9. Conclusions

The baroclinic response to tidal flow over the YP was investigated for a wide range of conditions including variations in tidal amplitude, tidal species, Coriolis frequency, stratification, and topography. This allowed for a determination of the many interesting regimes of IW generation in the area and the conditions necessary for the generation of ISWs.

The modeled barotropic tides forced by weak deep water currents (consistent with values derived from tidal models) did not result in the generation of ISWs. The baroclinic response forced by the K_1 tide is dominated by the second harmonic, in the form of coherent IW beams. This occurred as the slope near the shelf-break was critical for the $2\omega_{K_1}$ frequency. The slope criticality of the $2\omega_{K_1}$ frequency may therefore be a significant parameter for IW generation at high latitudes. The baroclinic response forced by the M_2 tide displayed a spectra of propagating IW beams at slightly superinertial frequencies.
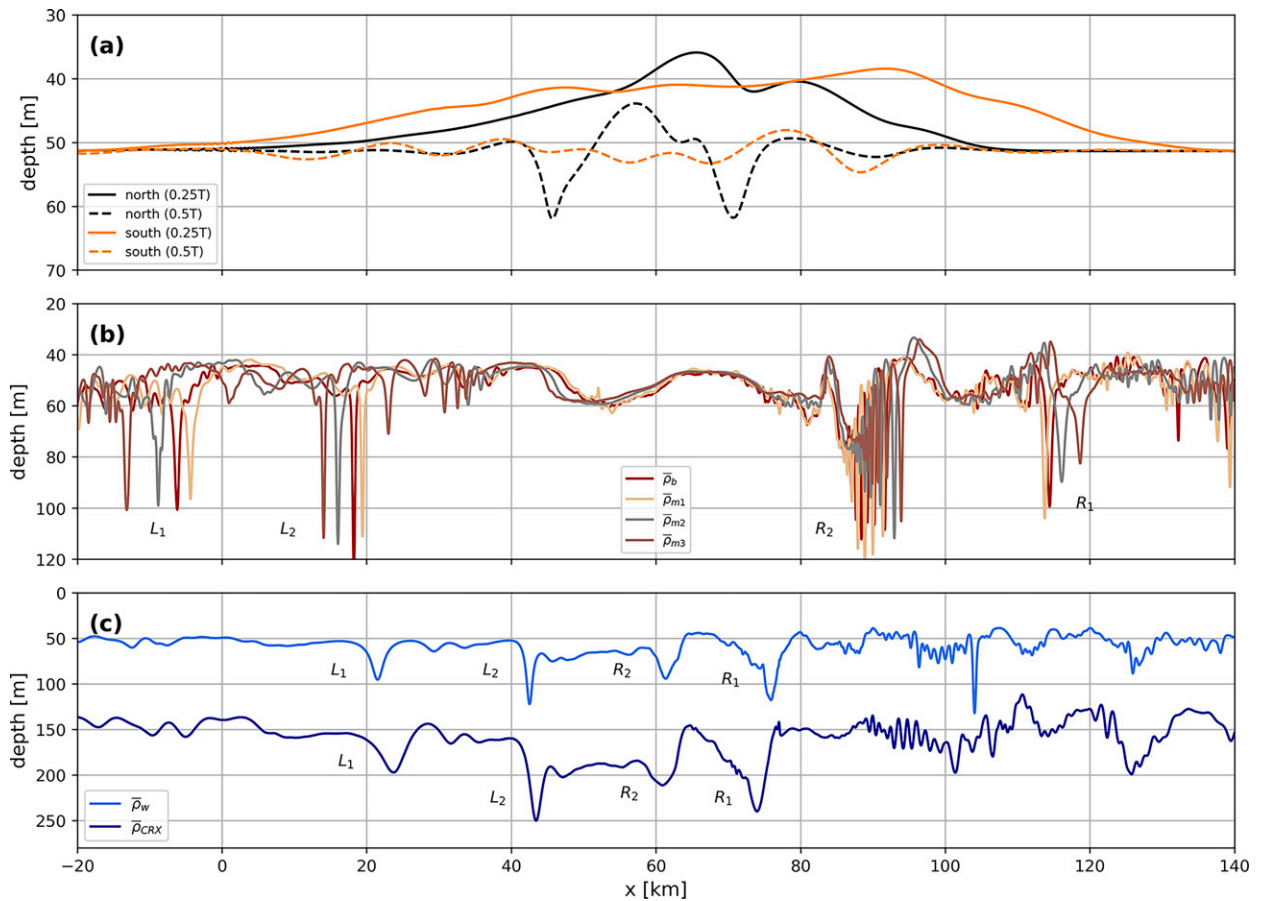
FIG. 12. Sensitivity results for the K_1 tide, $U_0 = 0.23$ m s^{-1}. (a) The 50-m isopycnal at $t = 0.25T$ and $t = 0.5T$ for the north and south transects. (b) The 50-m isopycnal at $t = 3T$ for the different summer stratifications. (c) Isopycnals at $t = 3.75T$ for the two winter stratifications. Isopycnal depths: 55 m for $\bar{\rho}_w$ and at 150 m for $\bar{\rho}_{\mathrm{CRX}}$.

The dominant frequencies generated are related to slope criticality of the topography. Further analytic and numerical studies are needed to improve the understanding of this novel IW generation mechanism, and to estimate their energy contribution to the Arctic Ocean.

When the barotropic tidal current amplitude is increased to levels observed over the YP during the presence of resonantly enhanced topographic vorticity waves, the response becomes nonlinear and ISWs are generated. These modeled ISWs are consistent with observations (section 2). The ISWs were generated for all the stratifications and Coriolis frequencies that we considered, although with some variations in their vertical structure and evolution. The presence and strength of enhanced diurnal currents is therefore a controlling factor in the

generation of ISWs. As the study used a proxy for the diurnal barotropic tides, 3D modeling is warranted to model both the topographic vorticity waves, the resulting baroclinic response, and the propagation and fate of the ISWs.

Changes in the Coriolis frequency, which we used as a proxy for changes in background vorticity, was found to have the potential to significantly increase the energy conversion from the M_2 tide. This was shown in the idealized setting of an f-plane (uniform background vorticity) and a single tidal constituent, while in reality there are multiple tidal constituents, as well as temporal and spatial scales to take into account. The lifespan, magnitude, and horizontal structure of background shear flows requires quantification. Localized background vorticity will trap the IW energy in the vicinity of the generation site resulting in

TABLE 3. Values of f used in the sensitivity runs for the K_1 tide, the corresponding ω_{K_1}/f values, the equivalent latitude, and the background vorticity required over the YP to have f_{eff} equal to f.

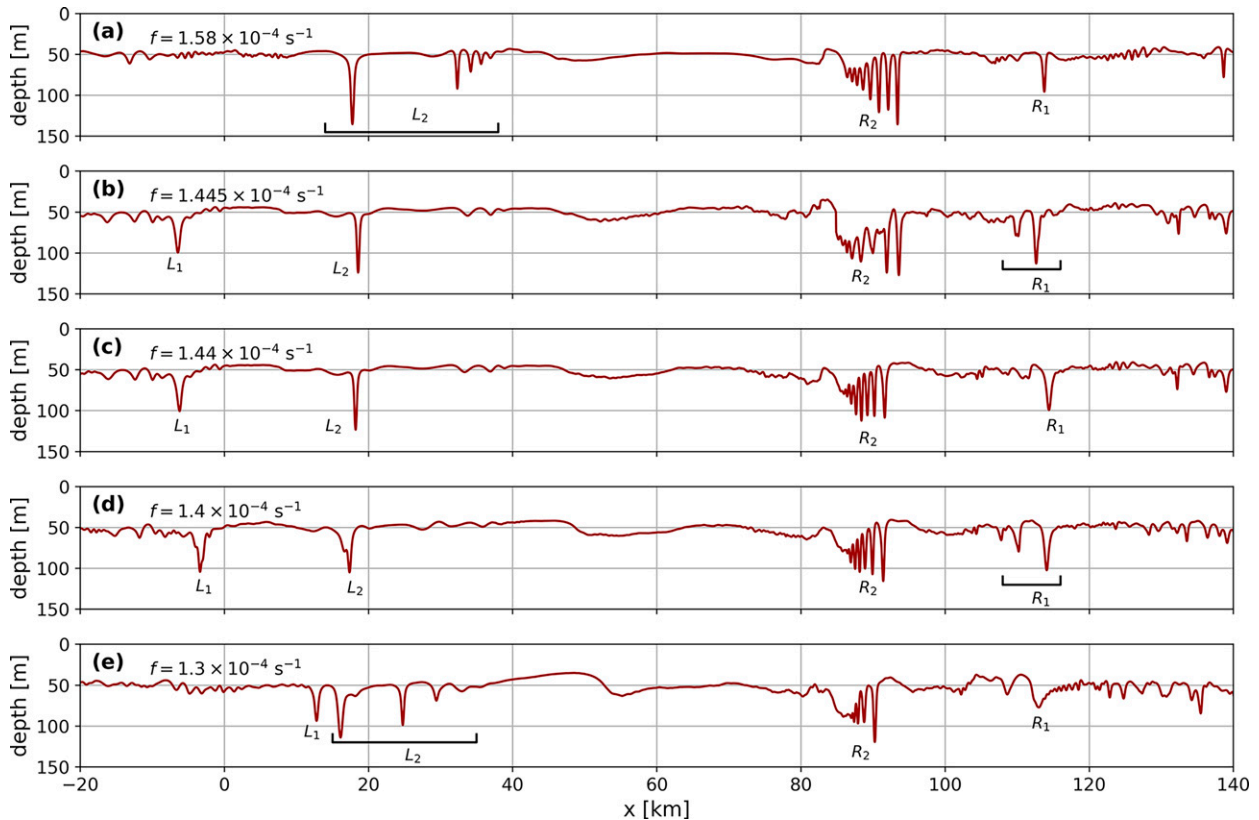| f (s^{-1})	1.3×10^{-4}	1.4×10^{-4}	1.44×10^{-4}	1.445×10^{-4}	1.58×10^{-4}
ω_{K_1}/f	0.561	0.521	0.506	0.505	0.462
Latitude (°)	63	73.8	80.9	82.2	—
ζ (s^{-1})	-2.66×10^{-5}	-7.89×10^{-5}	0	1.0×10^{-6}	2.94×10^{-5}

FIG. 13. Sensitivity to the Coriolis frequency. Results for the K_1 tide at $t = 3T$ for $U_0 = 0.23$ m s^{-1}. The 50-m depth isopycnal is shown. (a) $f = 1.58 \times 10^{-4}$ s^{-1}. (b) $f = 1.445 \times 10^{-4}$ s^{-1}. (c) $f = 1.440 \times 10^{-4}$ s^{-1} (base case). (d) $f = 1.400 \times 10^{-4}$ s^{-1}. (e) $f = 1.300 \times 10^{-4}$ s^{-1}.

local mixing events. Observational and 3D modeling studies are warranted to better understand the interaction between the general circulation and the internal tides.

The tidal dynamics over the YP is a useful case study for subinertial wave generation, which has direct impacts on the heat loss from the West Spitsbergen Current. An improved understanding of the tidal dynamics and nonlinear wave generation along the Arctic continental slopes will help improve estimates of the heat loss from the warm boundary current and the heat input into the Arctic Ocean.

Data availability statement. The data from CEAREX, presented in Fig. 2, are temporarily available (https://github.com/EarthAndSpaceResearch/CEAREX) until they are uploaded to the Arctic Data Center for archiving. The HM2015617 cruise data are available from Fer and Kolås (2018), through the Norwegian Marine Data Centre, https://doi.org/10.21335/NMDC-567625440; the 2007 and 2014 cruise data can be requested from the Norwegian Marine Data Centre (https://nmdc.no/). The PHC climatology is available at http://psc.apl.washington.edu/nonwp_projects/PHC/Climatology.html. AOTIM-5 and Gr1kmTM data are available through the Arctic Data Center with doi:10.18739/A2S17SS80 and doi:10.18739/A2251FM3S, respectively. Model data from the simulations presented in the results are available upon request.

REFERENCES

Aagaard, K., J. Swift, and E. Carmack, 1985: Thermohaline circulation in the Arctic Mediterranean Seas. *J. Geophys. Res.*, **90**, 4833–4846, https://doi.org/10.1029/JC090iC03p04833.

Baines, P. G., 1982: On internal tide generation models. *Deep-Sea Res.*, **29A**, 307–338, https://doi.org/10.1016/0198-0149(82)90098-X.

Bell, J. B., and D. L. Marcus, 1992: A second-order projection method for variable-density flows. *J. Comput. Phys.*, **101**, 334–348, https://doi.org/10.1016/0021-9991(92)90011-M.

Bell, T., 1975: Lee waves in stratified flows with simple harmonic time dependence. *J. Fluid Mech.*, **67**, 705–722, https://doi.org/10.1017/S0022112075000560.

Bourget, B., T. Dauxois, S. Joubaud, and P. Odier, 2013: Experimental study of parametric subharmonic instability for internal plane waves. *J. Fluid Mech.*, **723**, 1–20, https://doi.org/10.1017/jfm.2013.78.

Carmack, E., and Coauthors, 2015: Toward quantifying the increasing role of oceanic heat in sea ice loss in the new Arctic. *Bull. Amer. Meteor. Soc.*, **96**, 2079–2105, https://doi.org/10.1175/BAMS-D-13-00177.1.

Czipott, P. V., M. D. Levine, C. A. Paulson, D. Menemenlis, D. M. Farmer, and R. G. Williams, 1991: Ice flexure forced by internal wave packets in the Arctic Ocean. *Science*, **254**, 832–835, https://doi.org/10.1126/science.254.5033.832.

D'Asaro, E. A., and J. H. Morison, 1992: Internal waves and mixing in the Arctic Ocean. *Deep-Sea Res.*, **39A**, S459–S484, https://doi.org/10.1016/S0198-0149(06)80016-6.

Dosser, H. V., and L. Rainville, 2016: Dynamics of the changing near-inertial internal wave field in the Arctic Ocean. *J. Phys. Oceanogr.*, **46**, 395–415, https://doi.org/10.1175/JPO-D-15-0056.1.

——, M. Chanona, S. Waterman, N. Shibley, and M.-L. Timmermans, 2021: Changes in internal wave-driven mixing across the Arctic Ocean: Finescale estimates from an 18-year pan-arctic record. *Geophys. Res. Lett.*, **48**, e2020GL091747, https://doi.org/10.1029/2020GL091747.

Falahat, S., and J. Nycander, 2015: On the generation of bottom-trapped internal tides. *J. Phys. Oceanogr.*, **45**, 526–545, https://doi.org/10.1175/JPO-D-14-0081.1.

Fer, I., 2009: Weak vertical diffusion allows maintenance of cold halocline in the central Arctic. *Atmos. Ocean. Sci. Lett.*, **2**, 148–152, https://doi.org/10.1080/16742834.2009.11446789.

——, 2014: Near-inertial mixing in the central Arctic Ocean. *J. Phys. Oceanogr.*, **44**, 2031–2049, https://doi.org/10.1175/JPO-D-13-0133.1.

——, and E. Kolås, 2018: Ocean currents, hydrography and microstructure data from cruise HM2015617. Norwegian Marine Data Centre, accessed 10 February 2019, https://doi.org/10.21335/NMDC-567625440.

——, R. Skogseth, and F. Geyer, 2010: Internal waves and mixing in the marginal ice zone near the Yermak Plateau. *J. Phys. Oceanogr.*, **40**, 1613–1630, https://doi.org/10.1175/2010JPO4371.1.

——, M. Müller, and A. K. Peterson, 2015: Tidal forcing, energetics, and mixing near the Yermak Plateau. *Ocean Sci.*, **11**, 287–304, https://doi.org/10.5194/os-11-287-2015.

——, Z. Koenig, I. E. Kozlov, M. Ostrowski, T. P. Rippeth, L. Padman, A. Bosse, and E. Kolås, 2020: Tidally forced lee waves drive turbulent mixing along the Arctic Ocean margins. *Geophys. Res. Lett.*, **47**, e2020GL088083, https://doi.org/10.1029/2020GL088083.

Fine, E. C., and S. T. Cole, 2022: Decadal observations of internal wave energy, shear, and mixing in the western Arctic Ocean. *J. Geophys. Res. Oceans*, **127**, e2021JC018056, https://doi.org/10.1029/2021JC018056.

Garrett, C., 2001: What is the "near-inertial" band and why is it different from the rest of the internal wave spectrum? *J. Phys. Oceanogr.*, **31**, 962–971, https://doi.org/10.1175/1520-0485(2001)031<0962:WITNIB>2.0.CO;2.

——, and W. Munk, 1979: Internal waves in the ocean. *Annu. Rev. Fluid Mech.*, **11**, 339–369, https://doi.org/10.1146/annurev.fl.11.010179.002011.

——, and E. Kunze, 2007: Internal tide generation in the deep ocean. *Annu. Rev. Fluid Mech.*, **39**, 57–87, https://doi.org/10.1146/annurev.fluid.39.050905.110227.

Gerkema, T., and V. I. Shrira, 2005: Near-inertial waves on the "nontraditional" V plane. *J. Geophys. Res.*, **110**, C01003, https://doi.org/10.1029/2004JC002519.

——, F.-T. A. Lam, and L. R. M. Maas, 2004: Internal tides in the Bay of Biscay: Conversion rates and seasonal effects. *Deep-Sea Res. II*, **51**, 2995–3008, https://doi.org/10.1016/j.dsr2.2004.09.012.

Grimshaw, R. H., L. Ostrovsky, V. Shrira, and Y. A. Stepanyants, 1998: Long nonlinear surface and internal gravity waves in a rotating ocean. *Surv. Geophys.*, **19**, 289–338, https://doi.org/10.1023/A:1006587919935.

Guthrie, J., and J. Morison, 2021: Not just sea ice: Other factors important to near-inertial wave generation in the Arctic Ocean. *Geophys. Res. Lett.*, **48**, e2020GL090508, https://doi.org/10.1029/2020GL090508.

Helfrich, K. R., 2007: Decay and return of internal solitary waves with rotation. *Phys. Fluids*, **19**, 026601, https://doi.org/10.1063/1.2472509.

——, and W. K. Melville, 2006: Long nonlinear internal waves. *Annu. Rev. Fluid Mech.*, **38**, 395–425, https://doi.org/10.1146/annurev.fluid.38.050304.092129.

Howard, S. L., and L. Padman, 2021: Gr1kmTM: Greenland 1 kilometer Tide Model. Arctic Data Center, accessed 12 March 2022, https://doi.org/10.18739/A2251FM3S.

Hunkins, K., 1986: Anomalous diurnal tidal currents on the Yermak Plateau. *J. Mar. Res.*, **44**, 51–69, https://doi.org/10.1357/002224086788460139.

Jackson, C. R., J. C. Da Silva, and G. Jeans, 2012: The generation of nonlinear internal waves. *Oceanography*, **25**, 108–123, https://doi.org/10.5670/oceanog.2012.46.

Khatiwala, S., 2003: Generation of internal tides in an ocean of finite depth: Analytical and numerical calculations. *Deep-Sea Res. I*, **50**, 3–21, https://doi.org/10.1016/S0967-0637(02)00132-2.

Klymak, J. M., R. Pinkel, C.-T. Liu, A. K. Liu, and L. David, 2006: Prototypical solitons in the South China Sea. *Geophys. Res. Lett.*, **33**, L11607, https://doi.org/10.1029/2006GL025932.

Kolås, E., and I. Fer, 2018: Hydrography, transport and mixing of the West Spitsbergen Current: The Svalbard Branch in summer 2015. *Ocean Sci.*, **14**, 1603–1618, https://doi.org/10.5194/os-14-1603-2018.

Kolås, E. H., Z. Koenig, I. Fer, F. Nilsen, and M. Marnela, 2020: Structure and transport of Atlantic Water north of Svalbard from observations in summer and fall 2018. *J. Geophys. Res. Oceans*, **125**, e2020JC016174, https://doi.org/10.1029/2020JC016174.

Korobov, A., and K. G. Lamb, 2008: Interharmonics in internal gravity wave generated by tide-topography interaction. *J. Fluid Mech.*, **611**, 61–95, https://doi.org/10.1017/S0022112008002449.

Kowalik, Z., and A. Y. Proshutinsky, 1993: Diurnal tides in the Arctic Ocean. *J. Geophys. Res.*, **98**, 16 449–16 468, https://doi.org/10.1029/93JC01363.

Kozlov, I. E., E. V. Zubkova, and V. N. Kudryavtsev, 2017: Internal solitary waves in the Laptev Sea: First results of space-borne SAR observations. *IEEE Geosci. Remote Sens. Lett.*, **14**, 2047–2051, https://doi.org/10.1109/LGRS.2017.2749681.

Kundu, P. K., 1990: *Fluid Mechanics.* Academic Press, 638 pp.

Kunze, E., 1985: Near-inertial wave propagation in geostrophic shear. *J. Phys. Oceanogr.*, **15**, 544–565, https://doi.org/10.1175/1520-0485(1985)015<0544:NIWPIG>2.0.CO;2.

Kurkina, O., and T. Talipova, 2011: Huge internal waves in the vicinity of the Spitsbergen Island (Barents Sea). *Nat. Hazards Earth Syst. Sci.*, **11**, 981–986, https://doi.org/10.5194/nhess-11-981-2011.

Lamb, K. G., 1994: Numerical experiments of internal wave generation by strong tidal flow across a finite amplitude bank edge. *J. Geophys. Res.*, **99**, 843–864, https://doi.org/10.1029/93JC02514.

——, and V. T. Nguyen, 2009: Calculating energy flux in internal solitary waves with an application to reflectance. *J. Phys. Oceanogr.*, **39**, 559–580, https://doi.org/10.1175/2008JPO3882.1.

——, and M. Dunphy, 2018: Internal wave generation by tidal flow over a two-dimensional ridge: Energy flux asymmetries induced by a steady surface trapped current. *J. Fluid Mech.*, **836**, 192–221, https://doi.org/10.1017/jfm.2017.800.

Leaman, K. D., and T. B. Sanford, 1975: Vertical energy propagation of inertial waves: A vector spectral analysis of velocity profiles. *J. Geophys. Res.*, **80**, 1975–1978, https://doi.org/10.1029/JC080i015p01975.

Legg, S., 2014: Scattering of low-mode internal waves at finite isolated topography. *J. Phys. Oceanogr.*, **44**, 359–383, https://doi.org/10.1175/JPO-D-12-0241.1.

——, 2021: Mixing by oceanic lee waves. *Annu. Rev. Fluid Mech.*, **53**, 173–201, https://doi.org/10.1146/annurev-fluid-051220-043904.

Lenn, Y.-D., I. Fer, M.-L. Timmermans, and J. A. MacKinnon, 2022: Mixing in the Arctic Ocean. *Ocean Mixing*, M. Meredith and A. Naveira Garabato, Eds., Elsevier, 275–299, https://doi.org/10.1016/B978-0-12-821512-8.00018-9.

Levine, M. D., C. A. Paulson, and J. H. Morison, 1985: Internal waves in the Arctic Ocean: Comparison with lower-latitude observations. *J. Phys. Oceanogr.*, **15**, 800–809, https://doi.org/10.1175/1520-0485(1985)015<0800:IWITAO>2.0.CO;2.

Lincoln, B. J., T. P. Rippeth, Y.-D. Lenn, M. L. Timmermans, W. J. Williams, and S. Bacon, 2016: Wind-driven mixing at intermediate depths in an ice-free Arctic Ocean. *Geophys. Res. Lett.*, **43**, 9749–9756, https://doi.org/10.1002/2016GL070454.

MacKinnon, J. A., and Coauthors, 2017: Climate process team on internal wave–driven ocean mixing. *Bull. Amer. Meteor. Soc.*, **98**, 2429–2454, https://doi.org/10.1175/BAMS-D-16-0030.1.

Margolin, L. G., W. J. Rider, and F. F. Grinstein, 2006: Modeling turbulent flow with implicit LES. *J. Turbul.*, **7**, N15, https://doi.org/10.1080/14685240500331595.

Martini, K. I., H. L. Simmons, C. A. Stoudt, and J. K. Hutchings, 2014: Near-inertial internal waves and sea ice in the Beaufort Sea. *J. Phys. Oceanogr.*, **44**, 2212–2234, https://doi.org/10.1175/JPO-D-13-0160.1.

Mathur, M., G. S. Carter, and T. Peacock, 2016: Internal tide generation using green function analysis: To WKB or not to WKB. *J. Phys. Oceanogr.*, **46**, 2157–2168, https://doi.org/10.1175/JPO-D-15-0145.1.

Meyer, A., I. Fer, A. Sundfjord, and A. K. Peterson, 2017: Mixing rates and vertical heat fluxes north of Svalbard from Arctic winter to spring. *J. Geophys. Res.*, **122**, 4569–4586, https://doi.org/10.1002/2016JC012441.

Mohri, K., T. Hibiya, and N. Iwamae, 2010: Revisiting internal wave generation by tide-topography interaction. *J. Geophys. Res.*, **115**, C11001, https://doi.org/10.1029/2009JC005908.

Mooers, C. N. K., 1975: Several effects of a baroclinic current on the cross-stream propagation of inertial-internal waves. *Geophys. Fluid Dyn.*, **6**, 245–275, https://doi.org/10.1080/03091927509365797.

Morozov, E., and V. Paka, 2010: Internal waves in a high-latitude region. *Oceanology*, **50**, 668–674, https://doi.org/10.1134/S0001437010050048.

——, I. Kozlov, S. Shchuka, and D. Frey, 2017: Internal tide in the Kara Gates Strait. *Oceanology*, **57**, 8–18, https://doi.org/10.1134/S0001437017010106.

Munk, W., and C. Wunsch, 1998: Abyssal recipes II: Energetics of tidal and wind mixing. *Deep-Sea Res. I*, **45**, 1977–2010, https://doi.org/10.1016/S0967-0637(98)00070-3.

Nakamura, T., and T. Awaji, 2001: A growth mechanism for topographic internal waves generated by an oscillatory flow. *J. Phys. Oceanogr.*, **31**, 2511–2524, https://doi.org/10.1175/1520-0485(2001)031<2511:AGMFTI>2.0.CO;2.

——, ——, T. Hatayama, K. Akitomo, T. Takizawa, T. Kono, Y. Kawasaki, and M. Fukasawa, 2000: The generation of large-amplitude unsteady lee waves by subinertial K_1 tidal flow: A possible vertical mixing mechanism in the Kuril Straits. *J. Phys. Oceanogr.*, **30**, 1601–1621, https://doi.org/10.1175/1520-0485(2000)030<1601:TGOLAU>2.0.CO;2.

Nycander, J., 2005: Generation of internal waves in the deep ocean by tides. *J. Geophys. Res. Oceans*, **110**, C10028, https://doi.org/10.1029/2004JC002487.

Onarheim, I. H., L. H. Smedsrud, R. B. Ingvaldsen, and F. Nilsen, 2014: Loss of sea ice during winter north of Svalbard. *Tellus*, **66A**, 23933, https://doi.org/10.3402/tellusa.v66.23933.

Padman, L., and T. M. Dillon, 1987: Vertical heat fluxes through the Beaufort Sea thermohaline staircase. *J. Geophys. Res.*, **92**, 10 799–10 806, https://doi.org/10.1029/JC092iC10p10799.

——, and ——, 1991: Turbulent mixing near the Yermak Plateau during the coordinated eastern Arctic experiment. *J. Geophys. Res.*, **96**, 4769–4782, https://doi.org/10.1029/90JC02260.

——, and S. Erofeeva, 2004: A barotropic inverse tidal model for the Arctic Ocean. *Geophys. Res. Lett.*, **31**, L02303, https://doi.org/10.1029/2003GL019003.

——, T. Dillon, H. Wijesekera, M. Levine, C. Paulson, and R. Pinkel, 1991: Internal wave dissipation in a non-Garrett-Munk ocean. *Dynamics of Oceanic Internal Gravity Waves: Proc. 6th 'Aha Huliko'a Hawaiian Winter Workshop*, Honolulu, HI, University of Hawai'i at Mānoa, 31–51, http://www.soest.hawaii.edu/PubServices/1991pdfs/Padman.pdf.

——, A. J. Plueddemann, R. D. Muench, and R. Pinkel, 1992: Diurnal tides near the Yermak Plateau. *J. Geophys. Res.*, **97**, 12 639–12 652, https://doi.org/10.1029/92JC01097.

Rainville, L., and P. Winsor, 2008: Mixing across the Arctic Ocean: Microstructure observations during the Beringia 2005 expedition. *Geophys. Res. Lett.*, **35**, L08606, https://doi.org/10.1029/2008GL033532.

——, and R. A. Woodgate, 2009: Observations of internal wave generation in the seasonally ice-free Arctic. *Geophys. Res. Lett.*, **36**, L23604, https://doi.org/10.1029/2009GL041291.

Rippeth, T. P., B. J. Lincoln, Y.-D. Lenn, J. M. Green, A. Sundfjord, and S. Bacon, 2015: Tide-mediated warming of Arctic halocline by Atlantic heat fluxes over rough topography. *Nat. Geosci.*, **8**, 191–194, https://doi.org/10.1038/ngeo2350.

——, V. Vlasenko, N. Stashchuk, B. D. Scannell, J. M. Green, B. J. Lincoln, and S. Bacon, 2017: Tidal conversion and mixing poleward of the critical latitude (an Arctic case study). *Geophys. Res. Lett.*, **44**, 12–349, https://doi.org/10.1002/2017GL075310.

Shroyer, E., J. Moum, and J. Nash, 2010: Energy transformations and dissipation of nonlinear internal waves over New Jersey's continental shelf. *Nonlinear Processes Geophys.*, **17**, 345–360, https://doi.org/10.5194/npg-17-345-2010.

Skarðhamar, J., Ø. Skagseth, and J. Albretsen, 2015: Diurnal tides on the Barents Sea continental slope. *Deep-Sea Res. I*, **97**, 40–51, https://doi.org/10.1016/j.dsr.2014.11.008.

Smith, S. G. L., and W. Young, 2002: Conversion of the barotropic tide. *J. Phys. Oceanogr.*, **32**, 1554–1566, https://doi.org/10.1175/1520-0485(2002)032<1554:COTBT>2.0.CO;2.

Stastna, M., and K. G. Lamb, 2002: Large fully nonlinear internal solitary waves: The effect of background current. *Phys. Fluids*, **14**, 2987–2999, https://doi.org/10.1063/1.1496510.

Steele, M., R. Morley, and W. Ermold, 2001: PHC: A global ocean hydrography with a high-quality Arctic Ocean. *J. Climate*, **14**, 2079–2087, https://doi.org/10.1175/1520-0442(2001)014<2079:PAGOHW>2.0.CO;2.

Tanaka, Y., T. Hibiya, Y. Niwa, and N. Iwamae, 2010: Numerical study of K_1 internal tides in the Kuril straits. *J. Geophys. Res.*, **115**, C09016, https://doi.org/10.1029/2009JC005903.

Thorpe, S., 2021: The interaction of internal wave groups with a uniform sloping boundary. *J. Fluid Mech.*, **913**, A23, https://doi.org/10.1017/jfm.2020.1156.

Timmermans, M.-L., J. Toole, R. Krishfield, and P. Winsor, 2008: Ice-tethered profiler observations of the double-diffusive staircase in the Canada Basin thermocline. *J. Geophys. Res.*, **113**, C00A02, https://doi.org/10.1029/2008JC004829.

Vlasenko, V., N. Stashchuk, K. Hutter, and K. Sabinin, 2003: Nonlinear internal waves forced by tides near the critical latitude. *Deep-Sea Res. I*, **50**, 317–338, https://doi.org/10.1016/S0967-0637(03)00018-9.

Waterhouse, A. F., and Coauthors, 2014: Global patterns of diapycnal mixing from measurements of the turbulent dissipation rate. *J. Phys. Oceanogr.*, **44**, 1854–1872, https://doi.org/10.1175/JPO-D-13-0104.1.

Whalen, C. B., C. De Lavergne, A. C. Naveira Garabato, J. M. Klymak, J. A. Mackinnon, and K. L. Sheen, 2020: Internal wave-driven mixing: Governing processes and consequences for climate. *Nat. Rev. Earth Environ.*, **1**, 606–621, https://doi.org/10.1038/s43017-020-0097-z.

Wijesekera, H. W., L. Padman, T. Dillon, M. Levine, C. Paulson, and R. Pinkel, 1993a: The application of internal-wave dissipation models to a region of strong mixing. *J. Phys. Oceanogr.*, **23**, 269–286, https://doi.org/10.1175/1520-0485(1993)023<0269:TAOIWD>2.0.CO;2.

——, T. M. Dillon, and L. Padman, 1993b: Some statistical and dynamical properties of turbulence in the oceanic pycnocline. *J. Geophys. Res.*, **98**, 22 665–22 679, https://doi.org/10.1029/93JC02352.

Wunsch, C., and R. Ferrari, 2004: Vertical mixing, energy, and the general circulation of the oceans. *Annu. Rev. Fluid Mech.*, **36**, 281–314, https://doi.org/10.1146/annurev.fluid.36.050802.122121.

Zhang, S., and M. H. Alford, 2015: Instabilities in nonlinear internal waves on the Washington continental shelf. *J. Geophys. Res. Oceans*, **120**, 5272–5283, https://doi.org/10.1002/2014JC010638.

——, ——, and J. B. Mickett, 2015: Characteristics, generation and mass transport of nonlinear internal waves on the Washington continental shelf. *J. Geophys. Res. Oceans*, **120**, 741–758, https://doi.org/10.1002/2014JC010393.